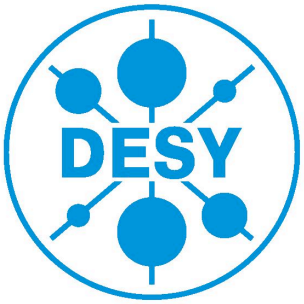

Dynamic Light Scattering Employing One- and Two-Dimensional Detectors and Different Time-Correlation Approaches

Summer Student Programme 2015

Ralf Klemt

University of Heidelberg

Germany

September 8, 2015

Supervisors:
Dr. Martin A. Schroer
Dr. Wojciech Roseker

Abstract

In this work, polystyrene microspheres with a nominal diameter of 1.93 µm and 4.52 µm are characterised by means of dynamic light scattering (DLS). A commercially available DLS setup containing a point detector for recording the scattered light is extended by a two-dimensional CCD detector, allowing for different correlation methods to be used and compared. In particular the analysis of speckle patterns enables both characterisation of the sample as well as of the beam properties. The validity of the assumption of free diffusion is checked and the hydrodynamic radius of the particles is determined to be $R_h = (1.03 \pm 0.03)$ µm for the smaller spheres and $R_h = (2.54 \pm 0.12)$ µm for the larger spheres. Based on the analysis of the correlation data, the application limits of dynamic light scattering methods for very large spheres (a diameter of 4.52 µm in this work) are discussed.

Contents

1 Introduction

Dynamic light scattering (DLS) is a key method to study the structural and dynamical properties of colloidal particle suspensions and has important applications in physics, chemistry and biology [1], for example in observing typical motility patterns of bacteria [2], or the size distributions of macromolecules and their interactions [3].
In this work, which was carried out in the context of the 2015 DESY summer student programme, solutions of polystyrene microspheres are characterised by means of dynamic light scattering and the analysis of so-called speckle patterns. DLS methods are usually applied to solutions of nanoparticles and the direct applicability to larger spheres is not necessarily given [1, 2, 4]. Therefore part of this work is to check the applicability for spheres with a diameter of 1.93 µm and 4.52 µm.
Section 2 gives an overview over the basic theory needed to understand dynamic light scattering and defines the correlation functions, which are directly or indirectly measured in an experiment. The experimental setup, the samples used and the measuring procedure are illustrated in section 3, while the analysis of the measured data is carried out in section 4. The analysis of the data taken with a standard DLS setup containing a point detector is illustrated in section 4.1, while the analysis of the speckle patterns recorded by a two-dimensional CCD camera and a comparison to the point detector data is shown in section 4.2. Finally section 5 presents a summary and conclusion over this work.

2 Theory

This section gives an overview over the most important theoretical results needed to understand the experimental findings. Unless stated otherwise, this section is based on [1].

2.1 Correlation Functions

The evaluation of light scattering experiments is strongly based on time correlation functions [1]. Therefore these are defined and introduced in this section.
To this end let $A(t)$ be some stochastic signal or function. The time average, i.e. the correlation function of first order, is defined as follows

$$\langle A(t)\rangle_t = \lim_{T\to\infty} \frac{1}{T} \int_t^T A(t')dt'. \tag{1}$$

For stationary signals, for example observables of systems in (thermal) equilibrium, the time average becomes time-independent and instead of $\langle A(t)\rangle_t$, $\langle A\rangle_t$ is written. In an experiment, a continuous measurement in the strict sense is of course not possible. Instead, the signal is recorded at several consecutive times t_j and the time average is

now given by

$$\langle A \rangle_t = \lim_{N\to\infty} \frac{1}{N} \sum_{j=1}^{N} A(t_j). \tag{2}$$

Equivalently, higher order correlation functions are defined as the time average of products of stochastic signals. As an important example, consider the time autocorrelation function

$$C_2 = \langle A(0)A(\tau) \rangle_t . \tag{3}$$

In the limit of $\tau \to 0$ the time autocorrelation function simplifies to $\langle A(0)A(0) \rangle_t = \langle A^2 \rangle_t$, giving an upper limit, while for long delay times $\tau \to \infty$ the measured signals (usually) get completely uncorrelated leading to $\langle A(0)A(\tau \to \infty) \rangle_t = \langle A(0) \rangle_t \langle A(\tau) \rangle_t = \langle A \rangle_t^2$ as a lower limit. A typical form of the time autocorrelation function is given by [1]

$$\langle A(0)A(\tau) \rangle_t = \langle A \rangle_t^2 + [\langle A^2 \rangle_t - \langle A \rangle_t^2] e^{-\frac{\tau}{\tau_r}} \tag{4}$$

where τ_r is the correlation or relaxation time. More generally one defines the relaxation time for an arbitrary form of time autocorrelation functions by

$$\tau_r = \int_0^\infty d\tau \frac{\langle \delta A(0) \delta A(\tau) \rangle}{\langle \delta A^2 \rangle} \tag{5}$$

where $\delta A(t) = A(t) - \langle A \rangle$.
In experiments usually time-averaged correlation functions are measured while in theory ensemble-averaged correlation functions are more accessible for calculations [1]. They are related by Birkhoff's ergodic theorem [5], stating that they are the same if the system is ergodic which is assumed henceforth.

2.2 Basic Light Scattering Theory

This subsection gives, based on [6], a short summary of some basic (static-) light scattering theory. Consider an incident electrical field in the form of a plane wave [1]

$$\mathbf{E}_i = \mathbf{n}_i E_0 e^{i(\mathbf{k}_i \cdot \mathbf{r} - \omega_i t)}, \tag{6}$$

in terms of the polarisation vector $\mathbf{n}_i$ of the wave, its amplitude E_0, wavevector k_i and frequency ω, illuminating a volume with a density of scattering centres $\rho(\mathbf{r})$ [2]. In the far field and applying the first Born approximation the scattered electrical field takes the form

$$E_f(\mathbf{r}') = E_i e^{i\mathbf{k}_i \mathbf{r}'} + E_i \frac{e^{ik_i r'}}{r'} r_0 \int_{Vol} \rho(\mathbf{r}) e^{i\mathbf{q}\mathbf{r}} d^3 r \tag{7}$$

[1] More realistic incident fields take the form of a superposition of several plane waves; however the spread in frequency is oftentimes negligible.

[2] In light scattering the scattering centres are predominantly electrons. Since we are not interested in the precise scattering mechanism here, a completely analogous treatment for scattering with for example neutrons is possible, where the scattering centres are nuclei.

in terms of the classical electron radius r_0, where one defines the form amplitude as

$$F(\mathbf{q}) = \int_{Vol} \rho(\mathbf{r}) e^{i\mathbf{qr}} d^3r. \tag{8}$$

In these equations $\mathbf{q}$ describes the wavevector transfer, $\mathbf{q} = \mathbf{k}_s - \mathbf{k}_i$, where $\mathbf{k}_{i/f}$ denotes the wavevector of the incident and the scattered light, respectively. Elastic scattering is assumed such that $|\mathbf{k}_i| = |\mathbf{k}_f|$. In this approximation the modulus of the wave vector transfer is given by

$$q = \frac{4\pi n}{\lambda} \sin \frac{\Theta}{2}, \tag{9}$$

where λ denotes the wavelength of the laser, n the index of refraction and Θ is the angle between $\mathbf{k}_i$ and $\mathbf{k}_s$.
Using the definition of the form amplitude, one arrives at the expression

$$\frac{d\sigma}{d\Omega}(\mathbf{q}) = r_0^2 F(\mathbf{q}) F(\mathbf{q})^* \tag{10}$$

for the differential cross section and

$$I(\mathbf{q}) = I_0 \frac{1}{L^2} \frac{d\sigma}{d\Omega}(\mathbf{q}) \tag{11}$$

for the scattered intensity. $I_0 = E_0^2$ denotes the intensity of the incident wave.
The next step is to go from a general distribution of scattering centres to a system of many - more precisely $\bar{N}$ on average - identical and radial-symmetric particles in the illuminated volume. Sufficient dilution, such that only single scattering has to be accounted for, is assumed. With the form amplitude $F_1(q)$ of the single particle, given in terms of the scattering centre distribution within one particle $\rho^{(p)}$ by

$$F_1(\mathbf{q}) = \int_{Vol} \rho^{(p)}(\mathbf{r}) e^{i\mathbf{qr}} d^3r \tag{12}$$

and the total density of scatteres

$$\rho(\mathbf{R}) = \sum_{j=1}^{\bar{N}} \rho^{(p)}(\mathbf{R} - \mathbf{R}_j), \tag{13}$$

where $\mathbf{R}_j$ denotes the centre of particle j, the total form amplitude is given by

$$F(q) = \sum_{j=1}^{\bar{N}} F_1(q) e^{i\mathbf{qR}_j}. \tag{14}$$

Making use of equations 10 , 11 and 14, the scattered intensity turns out to be given by

$$I(q) = I_0 \frac{r_0^2}{L^2} \bar{N} P(q) S(q) \tag{15}$$

in terms of the form factor $P(q)$ and the structure factor $S(q)$. The form factor accounts for the scattered light from each individual particle and is given by

$$P(q) = |F_1(q)|^2, \tag{16}$$

while the structure factor characterises correlations between the particles and is given by

$$S(q) = 1 + 4\pi \frac{\bar{N}}{V} \int_0^\infty r^2 (g(r) - 1) \frac{\sin qr}{qr} dr, \tag{17}$$

where $g(r)$ is the pair distribution function, that is, the probability of finding a particle at distance r from a given other particle. Note that in a more general approach it is possible to allow for anisotropic particles by introducing the form factor as averaged over orientations and replacing the structure factor by an effective one [6].
In this work diluted solutions of uncharged particles are considered. This implies that the particles can be assumed to be nearly non-interacting ($g(r) \to 1$) and therefore $S(q) \to 1$. Thus the structure factor is assumed to be equal to unity in the following.

2.3 Dynamic Light Scattering

In this subsection some basic results from dynamic light scattering (DLS) theory are summarized.
Light scattering experiments for relatively slow dynamic processes on timescales above 10^{-6} s usually rely on optical mixing techniques [1]. In this method the scattered light is recorded by a 'square-law detector', like a photo-diode or a CCD chip. If the scattered light is additionally superimposed with a local oscillator it is called a heterodyne method, otherwise a homodyne method. In both cases the count rate of the detector $n(t)$ at a certain time is proportional to the impinging light field,

$$n(t) \propto |E(t)|^2. \tag{18}$$

In optical mixing, the time autocorrelation of this signal is of interest, which is the output of some digital or analog (hardwire computer) correlator,

$$\langle n(0)n(\tau)\rangle \propto \langle |E(0)|^2 |E(t)|^2 \rangle \,. \tag{19}$$

In the special case of the homodyne method considered in this work, this is simply proportional to

$$I_2 = \langle |E_s(0)|^2 |E_s(t)|^2 \rangle \,. \tag{20}$$

It is not yet obvious on how to extract information on the dynamics out of this fourth moment of the scattered electrical field. It is possible, though, to simplify I_2 in the special case of 'Gaussian fields' [1]: To this end, assume that the effective scattering volume can be divided into several sub-regions, small in each dimension compared to the wavelength of light. In this case the total scattered field can be safely approximated

by the superposition of the mean value of the field originating from each individual region,

$$E_s = \sum_n E_s^{(n)}. \tag{21}$$

Assume further that on the one hand, each sub-volume is large enough to treat the motion of the particles independently, and that on the other hand, their total number is large enough to apply the central limit theorem to the scattered field. This means that the total scattered field, composed of many independent randomly distributed fields is itself randomly distributed according to a Gaussian. In general a Gaussian distribution is fully determined by its first two moments. Therefore the correlation function of fourth order I_2 can be related to correlation functions of first and second order by means of, for example, Wick's theorem [7],

$$I_2(t) = \langle |E_s|^2 \rangle^2 + \langle E_s^*(0) E_s(t) \rangle^2 . \tag{22}$$

Reintroducing the q dependence of the scattered field and defining the normalised correlation functions

$$g_1(q,t) = \frac{\langle E_s^*(q,0) E_s(q,t) \rangle}{\langle |E_s(q)|^2 \rangle}, \tag{23}$$

as well as

$$g_2(q,t) = \frac{\langle |E_s(q,0)|^2 |E_s(q,t)|^2 \rangle}{\langle |E_s(q)|^2 \rangle^2}, \tag{24}$$

leads to the important Siegert relation:

$$g_2(q,t) = 1 + \beta(q) |g_1(q,t)|^2. \tag{25}$$

As a slight generalisation to realistic experimental conditions, in the Siegert relation an additional coherence factor $\beta(q)$ (referred to as contrast as well), not present in the original Gaussian approximation, was introduced. It accounts for the (limited) coherence of the laser, and more importantly of the optics used. In light scattering experiments it is usually close to unity [1].

2.3.1 Diffusion

In order to relate the measured I_2 correlation function to the dynamics of the system the g_1 function has to be evaluated further. In this work diluted samples of large particles in the micrometer regime immersed in a fluid are considered. Their dynamics is well described by the translational self-diffusion model [8]. The basic assumptions are that the particles perform mutual independent translational movements, where the movement at any given point in time is independent of the movement and position at any earlier time [3]. The diffusion equation is given by

$$\frac{\partial P(\mathbf{r},t)}{\partial t} = D \nabla^2 P(\mathbf{r},t), \tag{26}$$

[3] That is, the particles perform a so-called random walk.

where $P(\mathbf{r}, t)$ is the probability density of a single particle being at $\mathbf{r}$ at time t and D is the translational diffusion coefficient for a spherical particle, given by the Stokes-Einstein relation [8],

$$D = \frac{kT}{6\pi\eta R_h} \tag{27}$$

in terms of the temperature T, the Boltzmann constant k, the solvent viscosity η and the (hydrodynamic) radius R_h of the particles.

2.3.2 Time Correlation Functions for Diffusing Particles

Using equation 14, still assuming that the particles are uncorrelated, g_1 takes a form according to

$$g_1(q,t) \propto \frac{1}{\bar{N}} \langle \sum_{j=1}^{N} b_j(0) b_j(t) e^{i\mathbf{q}[\mathbf{r}_j(t) - \mathbf{r}_j(0)]} \rangle \,. \tag{28}$$

Here the sum spans over all particles in the sample, not only those in the scattering area. To account for this the factors $b_j(t)$ where introduced, where $b_j(t)$ is defined to be unity if the particle j is in the scattering volume at time t and zero otherwise. Comparing the timescale on which a particles diffuses through the sample with the timescale the particle correlation falls off shows [1] that $b_j(0)b_j(t)$ varies much slower and therefore can be set to be equal to the value at $t = 0$ for all times, resulting in a factor of $b_j(0)b_j(0) = b_j(0)$ in equation 28. Furthermore, b_j is independent of the particle correlation and therefore:

$$g_1(q,t) \propto \frac{1}{\bar{N}} \sum_{j=1}^{N} \langle b_j(0) \rangle \langle e^{i\mathbf{q}[\mathbf{r}_j(t) - \mathbf{r}_j(0)]} \rangle = \sum_{j=1}^{N} \langle e^{i\mathbf{q}[\mathbf{r}_j(t) - \mathbf{r}_j(0)]} \rangle \,. \tag{29}$$

The correlation function $F_s = \langle e^{i\mathbf{q}[\mathbf{r}_j(t) - \mathbf{r}_j(0)]} \rangle$ is related to the probability distribution $G_s(\mathbf{R}, t)$ for a particle performing a displacement $\mathbf{R}$ in the time t via Fourier transformation,

$$FT[\langle e^{i\mathbf{q}[\mathbf{r}_j(t) - \mathbf{r}_j(0)]} \rangle] = \langle \delta(\mathbf{R} - [\mathbf{r}_j(t) - \mathbf{r}_j(0)]) \rangle = G_s(\mathbf{R}, t). \tag{30}$$

In the current approximation framework, for small concentrations [9], G_s is given as the solution of the diffusion equation

$$\frac{\partial G_s(\mathbf{R}, t)}{\partial t} = D \nabla^2 G_s(\mathbf{R}, t), \tag{31}$$

and accordingly

$$\frac{\partial F_s(\mathbf{q}, t)}{\partial t} = -q^2 D F_s(\mathbf{q}, t). \tag{32}$$

Therefore,

$$F_s(\mathbf{q}, t) = e^{-q^2 D t} = e^{-t/t_r}. \tag{33}$$

Finally, the g_2-function can be expressed in terms of the diffusion coefficient making use of equation 25,

$$g_2(q,t) = 1 + \beta(q) e^{-2q^2 D}. \tag{34}$$

Note that, at least for spherical particles, where no rotational motion has to be considered, the exact form of the form factor is of little interest, since it does not show up in the normalized g_2-function [2].

2.4 Speckle Patterns

Up to now the intensity at a fixed point in space was considered. This chapter focuses on the spatial distribution of the scattered light and is based on [10].
Coherent light impinging on a disordered system results in a random diffraction pattern known as 'speckle' pattern. While in a conventional DLS setup using a point detector only a small sector of the pattern on the order of a single speckle is analysed, a 'multispeckle analysis' takes the whole pattern into account. It is possible to extract information about the degree of coherence of the impinging radiation, as well as the (effective) illuminated volume size from a recorded speckle pattern as explained in the following [10]. Assuming full coherence, the probability distribution of the intensity in the speckle pattern is given in terms of the mean intensity by an exponential distribution [11]

$$P(I) = \frac{1}{\langle I \rangle} e^{-\frac{I}{\langle I \rangle}}. \tag{35}$$

A generalisation to partial coherence, i.e. to sample volumes consisting of M coherence volumes, leads to

$$P_M(I) = M^M \left(\frac{I}{\langle I \rangle} \right)^{M-1} \frac{e^{\frac{-MI}{\langle I \rangle}}}{\Gamma(M) \langle I \rangle} \tag{36}$$

in terms of the Euler Γ-function. This allows for a different expression for the coherence factor β. It is given by

$$\beta = \frac{\sigma(I)}{\langle I \rangle} \tag{37}$$

where the standard deviation σ of the intensity may be expressed in terms of M by

$$\sigma = \frac{\langle I \rangle}{\sqrt{M}}, \tag{38}$$

resulting in

$$\beta = \frac{1}{\sqrt{M}}. \tag{39}$$

In addition to the intensity distribution, in the speckle pattern the size of the individual speckles in the far field is of interest. It is given by

$$\delta x = \lambda \frac{L}{D} \tag{40}$$

where δx is the full width at half maximum in one direction, D the effective scattering region in this direction and L the sample detector distance. The speckle size is independent of the particle size; however in the limit of multiple scattering (i.e. turbid samples) the effective scattering volume increases (large q-values from the first scattering process may be rescattered to lower q-values) and accordingly the speckle size decreases [12].

3 Experiment

In this work several samples of polystyrene microspheres are characterised by dynamic light scattering techniques. This includes both measurements with an avalanche photo-diode (APD) and two-dimensional measurements of speckle patterns with a CCD camera. This section outlines the experimental setup and the general measurements procedure.

3.1 Experimental Setup

The DLS setup used in this work is sketched in figure 1.
It is based on the 3D DLS spectrometer from *LSinstruments*[4]. The setup consists of a HeNe cw-laser as a light source, and a tunable filter to attenuate the laser beam accounting for different scattering intensities of different samples and different angles. The specifications of the laser are given in table 1. Note that the original setup is capable of cross-correlation measurements, and therefore the beam path is split. In this work only one of the paths is used, while the other one is blocked.

Parameter	**HeNe laser**
Wavelength λ	632.8 nm
Power P	22 mW
Beam diameter $(1/e^2)$	0.7 mm
Beam divergence	1.15 mrad
Polarization ratio	500 : 1 (vertical)

Table 1: Specifications of HeNe laser.

The sample, contained in a 10 mm diameter glass cuvette, is placed in an index-matching cis/trans-decalin bath to avoid unwanted scattering from the cuvette walls. Scattered light is focused into an avalanche photo-diode (APD), which is connected to a multitau-correlator giving the auto-correlation function. The sample is temperature monitored using a Pt-100 temperature sensor.
The photo-diode is placed on a goniometer arm, capable of scanning an angular range of 16° to 148°. The setup was extended by mounting, in addition to the photo-diode, a *Basler Aviator avA 1000-120km* CCD camera[5] on the goniometer arm, to allow for recording two-dimensional speckle patterns. The specifications of the CCD camera are given in table 2. The CCD is connected via a camera link interface to a computer. To avoid stray light, the camera is carefully shielded by a light absorbing cover. Furthermore, for each measurement with the CCD camera, a couple of dark frames are taken as well, and their mean is subtracted from the recorded images.

[4]LS instruments AG, Fribourg, Switzerland
[5]Basler AB, Ahrensburg, Germany

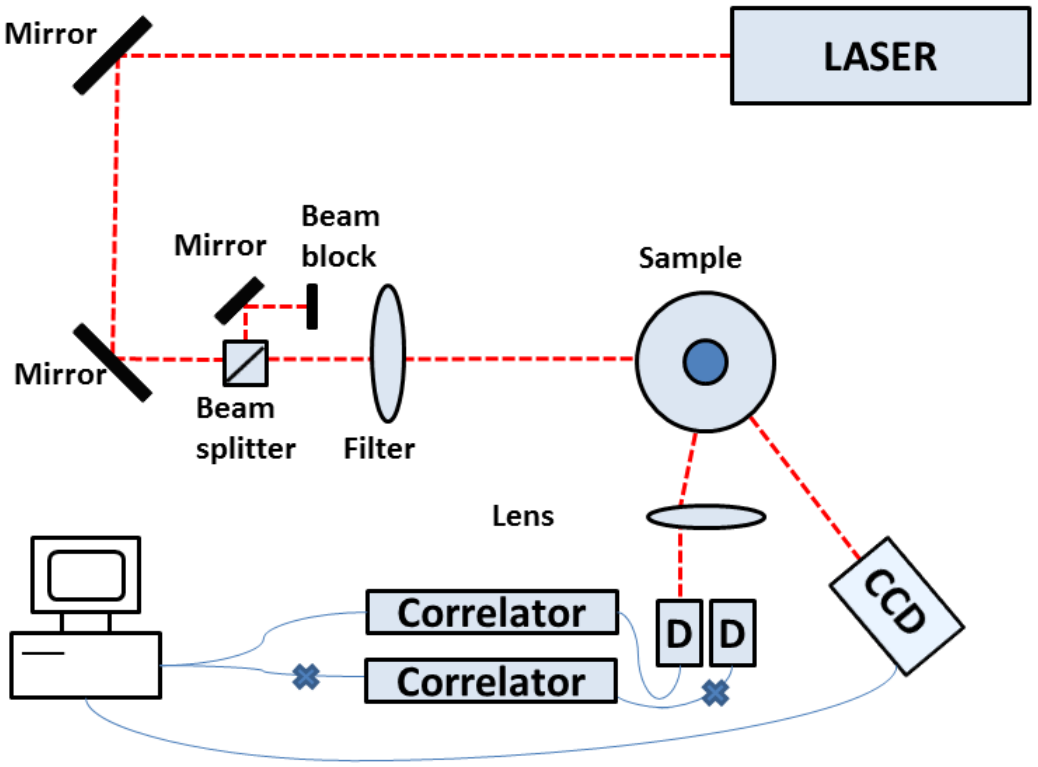

Figure 1: Sketch of the experimental setup. The setup is capable of cross-correlation measurements. Therefore the light from the laser is reflected into a beam splitter. In the original setup, both beams are focused on the sample and the scattered light is detected by two photo-diodes (here marked by D) and for both diodes the correlation is calculated. This work does not rely on cross-correlation measurements. For this reason, one of the beams was blocked and only one photo-diode and correlator used. The setup was extended by mounting an additional CCD detector next to the diodes.

Parameter	Basler Aviator
Pixel	1024 x 1024
Pixel size	5.5 x 5.5 µm
Dynamic range	8 bit
Max. frame rate	120 fps
Sensor type	Kodak KAI-1050
Sensor techn.	Progressive scan CCD, global shutter

Table 2: Specifications of Basler Aviator CCD Camera.

3.2 Sample preparation

All the samples in this work consist of polystyrene spheres solved in water. The spheres used are *Polybead Polysterene Microspheres* [6] (2.5 % by volume polystyrol spheres in water) with a diameter of approximately 2 µm and 4.5 µm, respectively. The specifications of the spheres are given in table 3

Solution	Diameter	standard deviation	concentration
2 µm Microspheres	1.93 µm	0.05 µm	$\approx 5.9 \times 10^9\,\mathrm{ml}^{-1}$
2 µm Microspheres	4.52 µm	0.15 µm	$\approx 5.0 \times 10^8\,\mathrm{ml}^{-1}$

Table 3: Specifications of microspheres.

The samples are prepared by pipetting a certain amount of polystyrene sphere solution and purified water into a cuvette with 10 mm diameter. The cuvette is carefully cleaned (from the inside) beforehand and purified water is used. In principle isopropanol can be used to clean the cuvettes. However it proved to be hard to fully evaporate the isopropanol (see section 4.1.4) and therefore the cuvettes are cleaned with water alone in all measurements unless stated otherwise.
To have a good homogeneity the samples are mixed with a vortex mixer as well as an ultrasonic bath. Furthermore, the samples are centrifuged to get rid of small bubbles within the solution that lead to additional parasitic scattering. However, the time in the centrifuge is kept short enough (≈ 15 s) and the rotation speed slow enough (1000 rpm) to avoid sedimentation of the microspheres. Scattering from the wall of the cuvette is further minimized by cleaning it from the outside with ethanol.
The concentration of spheres in water is chosen low enough, such that the approximation of single scattering, which is central to the scattering theory developed in the previous sections, holds. Nevertheless enough spheres have to be present in the scattering volume to use all the statistical properties, for example in deriving the Siegert relation (equation 25). Fulfilling both requirements gets increasingly problematic for larger particles. For this reason samples with two different concentrations of polystyrene spheres are prepared and are compared in the analysis.

[6] Polysciences, Inc., Warrington, USA

Table 4 gives an overview over all the samples used, and the names they are referred to henceforth.

Name	Size of spheres	Polystyrene	Water	Isopropanol
2 µm PS DL0	2 µm	3 µl	3000 µl	No
2 µm PS DL1	2 µm	1 µl	3000 µl	No
4.5 µm PS DL0	4.5 µm	20 µl	3000 µl	No
4.5 µm PS DL1	4.5 µm	5 µl	3000 µl	No
2 µm PS DL1 + Iso.	2 µm	1 µl	3000 µl	Yes
Water + Iso.	-	0 µl	3000 µl	Yes

Table 4: Overview over the samples used.

3.3 Measurements

In table 5 all the measurements performed are summarized. The output of the DLS setup with the point detector, i.e. both the instantaneous count rate and the autocorrelation function, is saved in an ASCII data file, while the data taken by the CCD is saved as a png-image. Both data types are analysed and evaluated using MATLAB.

Number	Sample	Detector	angles
1	2 µm PS DL1	APD	30° - 130° (1° stepsize)
2	4.5 µm PS DL1	APD	30° - 130° (1° stepsize)
3	4.5 µm PS DL0	APD	30° - 130° (1° stepsize)
4.1	2 µm PS DL0	APD	15° - 130° (1° stepsize)
4.2	2 µm PS DL0	APD	15°,20°,25°,30°,35°,40°,50°
5.1	4.5 µm PS DL0	APD	15° - 130° (1° stepsize)
5.2	4.5 µm PS DL0	APD	15°,20°,25°,30°,35°,40°,45°,50°

Table 5: Overview over all measurements.

4 Analysis

To extract information about size and dynamics of the microspheres, the recorded data are analysed. Section 4.1 focuses on the data from the point detector, whereas section 4.2 explains the analysis of the two-dimensional speckle patterns.

4.1 Static and Dynamic Light Scattering

4.1.1 2 µm polystyrene spheres

The first measurement is the characterisation of the 2 µm polystyrene spheres. Data were taken with the DLS setup in an angular range from 30° to 130° in steps of 1°, with

a measurement time of 60 s each. The temperature was set to $(22.3 \pm 0.1)\,°C$.
Figure 2a shows, as an example, the measured g_2-function for the full time-scale measured plotted in semi-logarithmic scale for an angle of 40°.

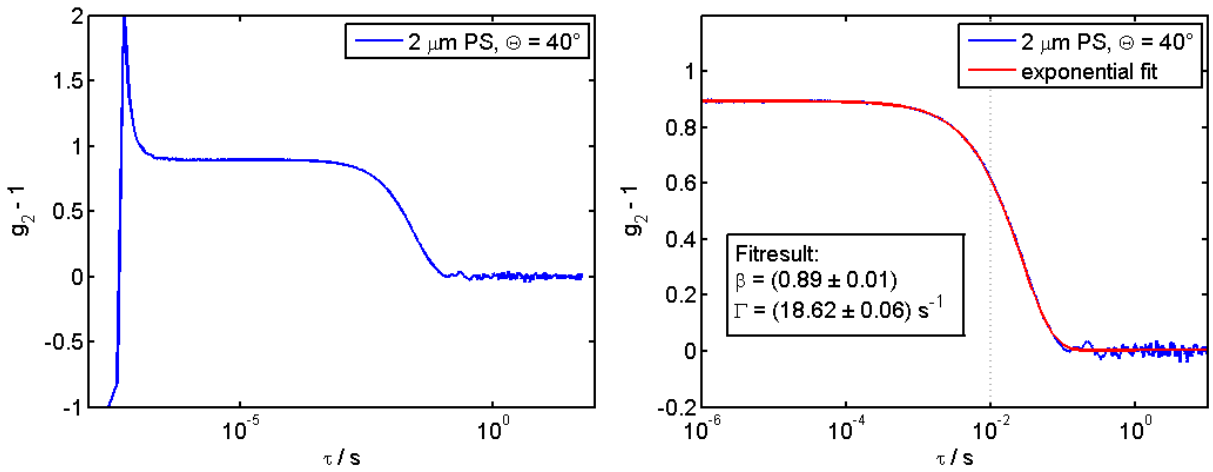

(a) Full range (b) Limited range and fit to data

Figure 2: Measured g_2-function of 2 µm polystyrene spheres at 40°.

According to theory (see equation 34) an exponential decrease of correlation from an initial value of $\beta \lesssim 1$ is expected. Indeed, for a time range from 10^{-6} s to 10^{-1} s, this seems to be the case. For very low times, due to the finite time resolution of the detector, the correlation function starts to build up from a value of zero. For a delay time τ around $\tau \approx 10^{-7}$ s the g_2-function exceeds the value of 1, which is clearly in contradiction to equation 34. This can be explained by the limited time resolution of the detector in addition to possible incoherent background by e.g. the optics in the setup. Furthermore, in principle scattering by both the solute and the solvent has to be considered. The water molecules are of course much smaller and their correlation function decays on a much shorter timescale. Therefore, by excluding very small times ($\tau \gtrsim 10^{-6}$), equation 34, with β replaced by $\beta_{app} = \beta(\frac{I_{solute}}{I_{solution}})^2$, is recovered [9]. However, the scattered intensity of the water is much lower than the intensity scattered by the spheres, such that $\beta_{app} \approx \beta$.
For larger times $\tau \gtrsim 10^{-1}$ s fluctuations show up. Some fluctuations are expected, because of decreasing statistics (e.g. for 1 s, the averaging process includes a solely 59 single measurements) and possible effects from non-Gaussian statistics. This is because in deriving the Siegert relation, the scattered field in equation 21 was approximated by a Gaussian. This approximation breaks down for particles larger than the wavelength of the laser, which is indeed the case here. In [4] it was shown, though, that the resulting effect of non-Gaussian fluctuations of the concentration leads only to an additional background for larger values of the delay time, leaving the central content of the Siegert relation valid. A further discussion of fluctuations at large τ is postponed to section 4.1.3 in the context of the larger 4.5 µm spheres at very low concentrations, where fluctuations

are even more apparent.
For the reasons stated above, fitting of the g_2-function is restricted to the range of $10^{-6}\,\mathrm{s}$ to $10^{-2}\,\mathrm{s}$. The exponential fit corresponding to the data in figure 2a is shown in figure 2b. The dotted vertical line indicates the longest time still accounted for in the fit. With the limitation to the given time range the fit is of good quality, which is supported by an adjusted R^2-value of $R^2 = 0.9995$. From the fit the corresponding values for the contrast $\beta = 0.89 \pm 0.01$ and the relaxation rate $\Gamma = (18.62 \pm 0.06)\,\mathrm{s}^{-1}$ are determined.
In order to determine the hydrodynamic radius of the spheres and to check the assumption of free diffusion, the relaxation rate has to be determined for different values of the scattering angle. Figure 3 shows some examples of the resulting fits to the data. It is clearly visible that the relaxation rate is decreasing with increasing angle, since for a larger wavevector transfer a smaller distance is resolved.
Most of the fits are of very good quality (more then 90% of the adjusted R^2-values are above 0.95; the minimum value is $R^2 = 0.869$). The next step is to relate the scattering angle to the wavevector transfer q. With the given wavelength of the laser and the index of refraction of water $n = 1.33$ [13], these are related by equation 9. Figure 4 shows the relaxation rate Γ plotted against the q^2-value. Assuming free diffusion, according to equation 34, a linear behaviour is expected with a slope of

$$\frac{\Gamma}{q^2} = 2D. \tag{41}$$

A linear regression of the data supports the assumption of linear behaviour with a goodness of fit of $R^2 = 0.993$. The resulting diffusion coefficient is given by $D = (2.23 \pm 0.01) \times 10^{-13}\,\mathrm{m}^2/\mathrm{s}$. According to equation 27 the hydrodynamic radius can be calculated if the viscosity and the temperature are known. The temperature was directly measured, while the viscosity, being a function of the temperature itself, is given for example in [14]. This results in a hydrodynamic radius of

$$R_h = (1.03 \pm 0.03)\,\mu\mathrm{m}$$

to be compared with the particle radius according to the manufacturer of

$$R = (0.97 \pm 0.03)\,\mu\mathrm{m}.$$

The measured hydrodynamical radius is comparable to the nominal one. A complete equivalence is not to be expected, since the hydrodynamical radius is an effective radius which accounts for a possible 'solvent-shell' around the particles as well.
Due to the facts that the data follows the assumed linear behaviour closely and that a second measurement with slightly higher concentrations gives compatible results (see section 4.2.2) it can be assumed that the relevant assumptions on free diffusion and single scattering are valid. Note however, that for micrometer sized particles, this is only the case for spherical particles. To illustrate this the median of the total scattered intensity is plotted against the wavevector transfer in figure 5.
In arbitrary scaling the form factor in the approximation scheme used in section 2 (which is in its combined form called Rayleigh-Gans-Debye (RGD) approximation) is plotted as

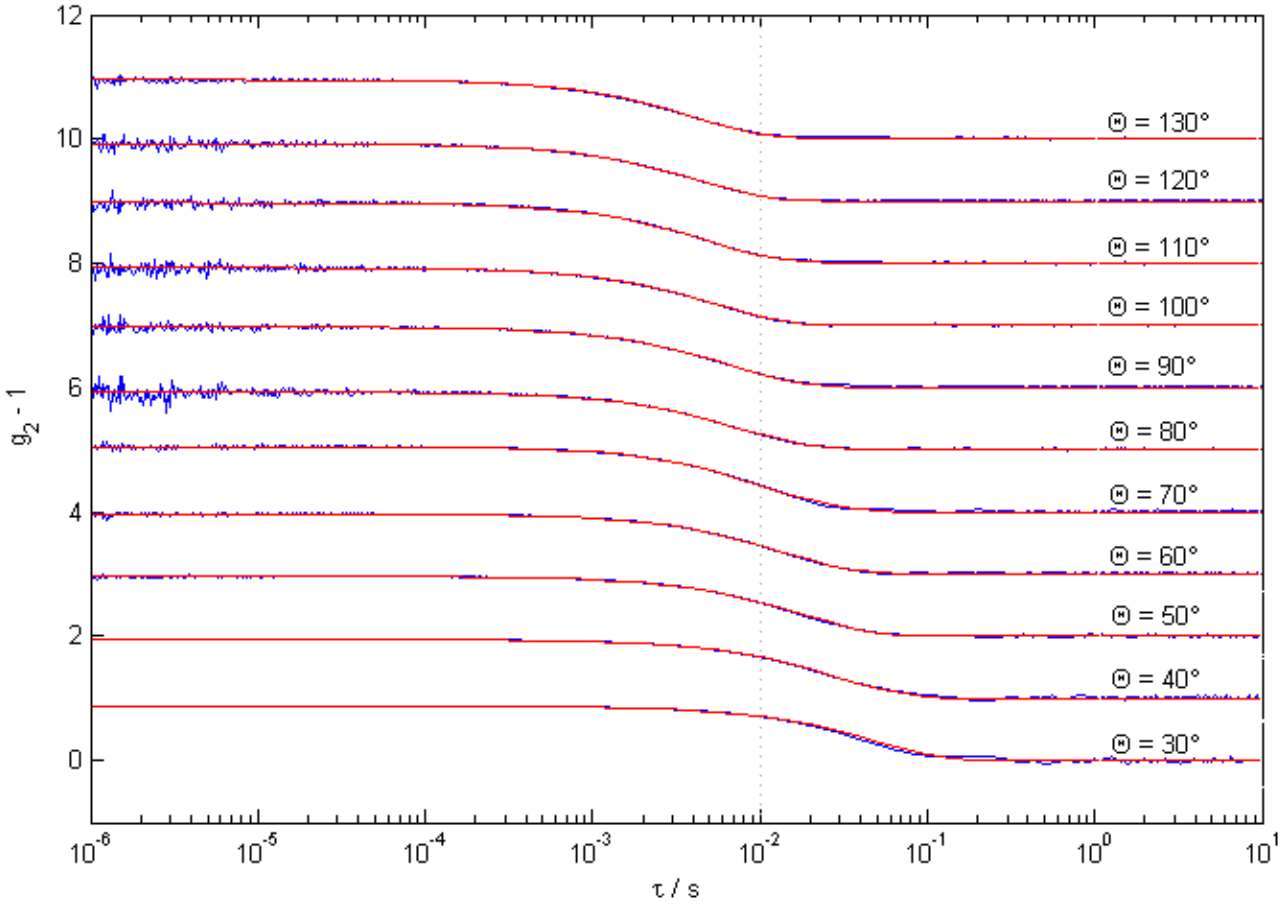

Figure 3: Measured g_2-functions of 2 µm polystyrene spheres in the angular range of 10° to 130° with corresponding fits to the data. The curves were shifted vertically for clarity.

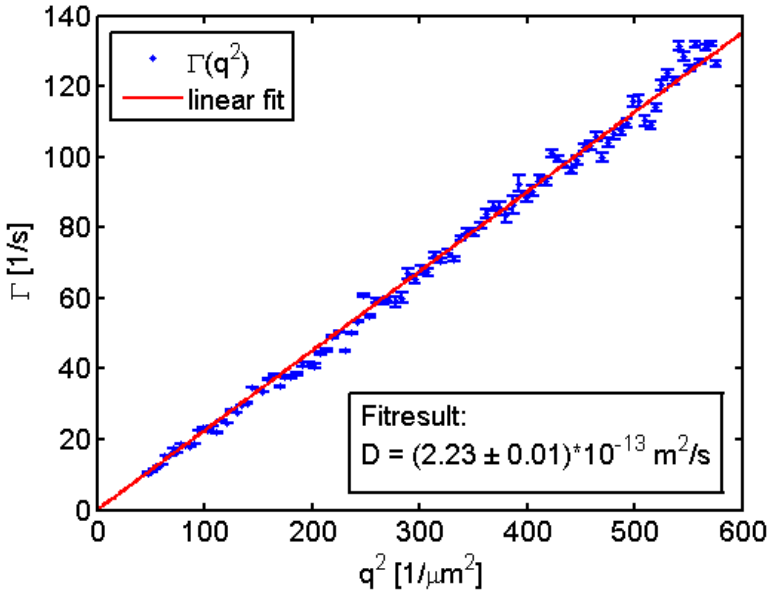

Figure 4: Dependence of the relaxation rate on the q^2-value for 2 µm polystyrene spheres and a corresponding linear regression.

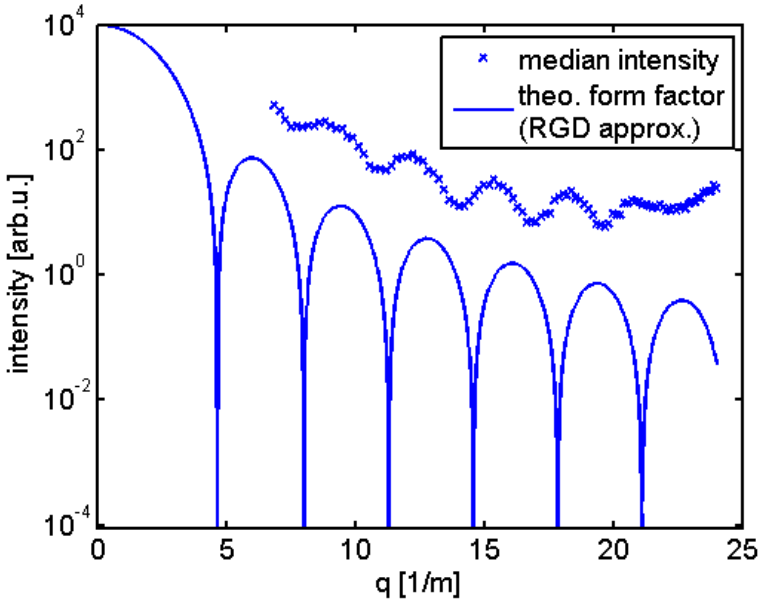

Figure 5: Dependence of the median of the scattered intensity from 2 µm polystyrene spheres on the wavevector transfer and the theoretical curve according to Rayleigh-Gans-Debye theory for spheres of radius $R = 0.97$ in arbitrary scaling.

well [7]. The RGD approximation assumes that the quotient m of the refractive indeces of particles and solution is close to one ($|m-1| \ll 1$) and that the phase difference of light with wavevector k travelling through the particle with radius R and light passing by is small ($2kR|m-1| \ll 1$) [2]. Both requirements are clearly not met by polystyrene microspheres (index of refraction of about 1.6). Therefore it is not surprising, that the form factor in figure 5 is not able to describe the intensity curve correctly [8]. Some features, especially the general decrease of intensity with increasing angle as well as the oscillations in the intensity are present in both theory and experimental data, though. Note however that back-scattering is not accounted for in the theoretical form factor shown here, but leads to an increase of intensity at wide angles in the experimental data and that the oscillations are not fully resolvable due to the finite angle resolution.
For spheres the lack of a proper description of the form factor has no impact on the time autocorrelation functions determined above, because the g_2-function is normalized by the mean scattered intensity into the different angles [2]. This is not true for non-spherical particles, where rotational motions and therefore a change of the form factor at a certain fixed angle has to be considered. Therefore, for nonspherical particles in the micrometer regime, the theory has to be extended in terms of the exact scattered intensity distribution [1, 2].

4.1.2 4.5 µm polystyrene spheres

In principle the same procedure as in section 4.1.1 can be used to determine the hydrodynamical radius of the 4.5 µm polystyrene spheres. In this section the higher concentrated 4.5 µm PS DL0 sample is used. Approximately $\mathcal{O}(10^4)$ of spheres are in the scattering volume at all times, ensuring at least an approximate validity of the assumed many-particle limit. Nevertheless, the results have to be treated carefully, since the solution is already slightly opaque at such high concentration and the single scattering limit holds now only approximately true.
Figure 6 shows the measured g_2-function, with very low times already excluded, and a fitted curve according to equation 34.
As before, some fluctuations for larger delay times are visible. These will be further discussed in the context of very low concentrations (section 4.1.3). For now, the range of fitting is restricted to 10^{-6} s to 5×10^{-2} s [9]. For this range the fit is, with an adjusted R^2-value of $R^2 = 0.998$, of good quality.
Figure 7 shows some examples of the g_2-functions over the whole angular range, including the corresponding fits.
Overall the fits are of good quality with a minimum adjusted R^2-value of $R^2 = 0.85$. However, for some of the correlation functions, the contrast determined by the fit lies above 1. This is a relict of the finite averaging time, when for a short time the scattered

[7] It is given in terms of the sphere radius R by $P(q) = \left(3\frac{\sin(qR) - qR\cos(qR)}{q^3R^3}\right)^2$.
[8] For this, so-called Mie scattering has to be considered.
[9] Compared to the 2 µm particles, the fit range was slightly extended, accounting for the overall slower dynamics.

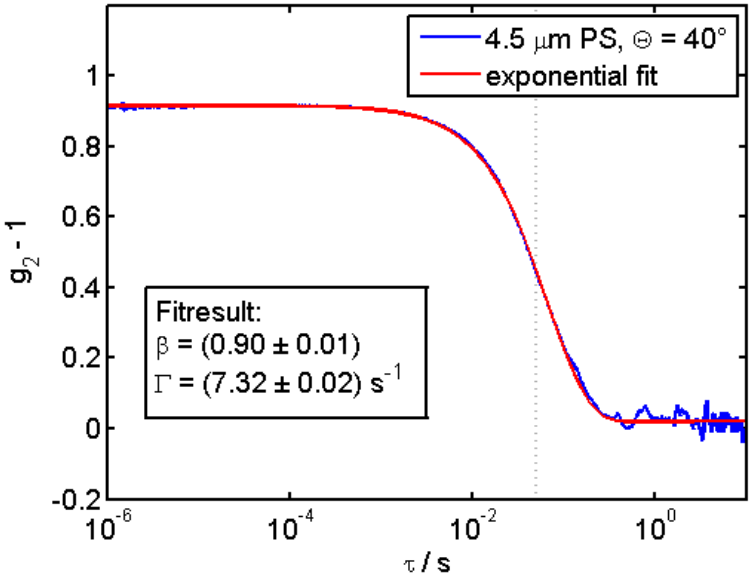

Figure 6: Measured g_2-function of 4.5 µm polystyrene spheres at 40° and a fit to the data.

intensity was surpassing the average significantly. These fits were excluded in the following.

The next step is again to determine the hydrodynamic radius. Figure 8 shows the decay rate Γ determined by the fit, plotted against the squared wavevector transfer q^2. Overall, the relaxation rate approximately follows the expected linear behaviour and the fit quality is good ($R^2 = 0.988$). This supports the assumption that multiple scattering is still negligible using this concentration. The linear regression yields a diffusion coefficient of $D = (9.04 \pm 0.05) \times 10^{-14}\,\mathrm{m}^2/\mathrm{s}$, resulting in a hydrodynamic radius of

$$R_h = (2.53 \pm 0.12)\,\mu\mathrm{m} \tag{42}$$

to be compared with the particle radius according to the manufacturer of

$$(2.26 \pm 0.08)\,\mu\mathrm{m}. \tag{43}$$

The radii are compatible within the 3σ range. However, it is pointed out again that complete equivalence between hydrodynamic and nominal radius is not to be expected. As for the smaller spheres, in figure 9 the median scattered intensity and the form factor in RGD approximation are shown. For larger particles, the oscillations in q-space have a higher frequency. For this reason, no clear structure in the experimental data is visible anymore due to the finite resolution. Nevertheless, the considerations made above for applicability and effects of the RGD approximations apply to the larger 4.5 µm spheres as well.

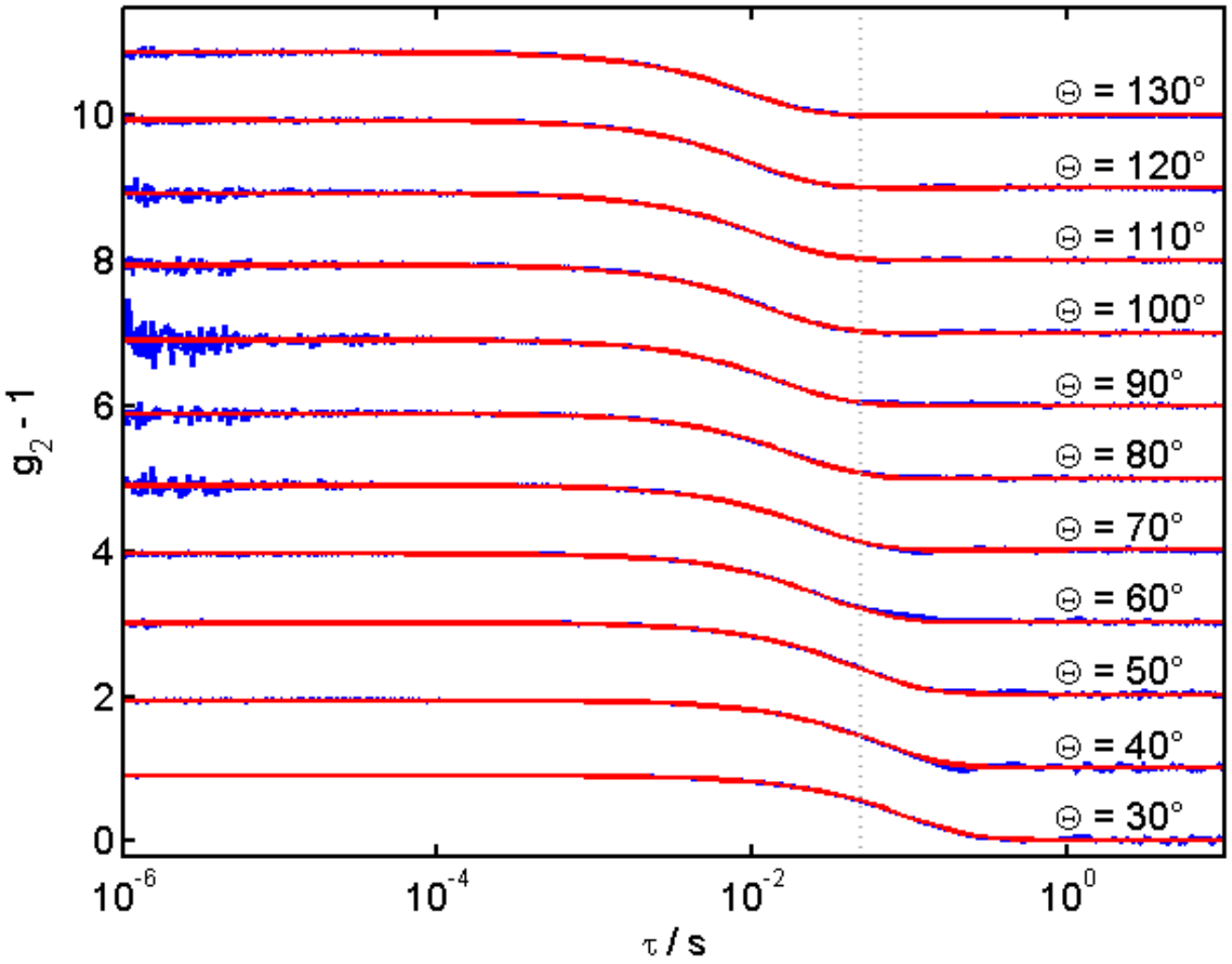

Figure 7: Measured g_2-functions of 4.5 µm polystyrene spheres in the angular range of 10° to 130° with corresponding fits to the data.

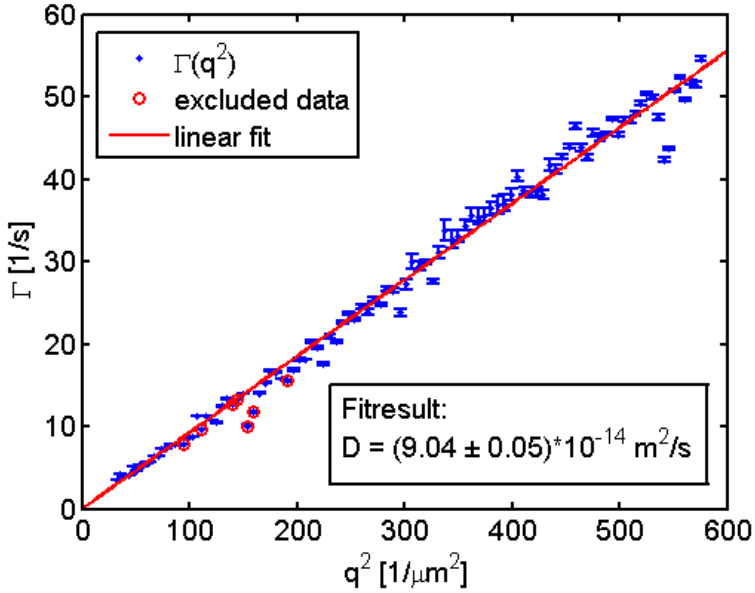

Figure 8: Dependence of the relaxation rate on the q^2-value for 4.5 µm polystyrene spheres and a corresponding linear regression.

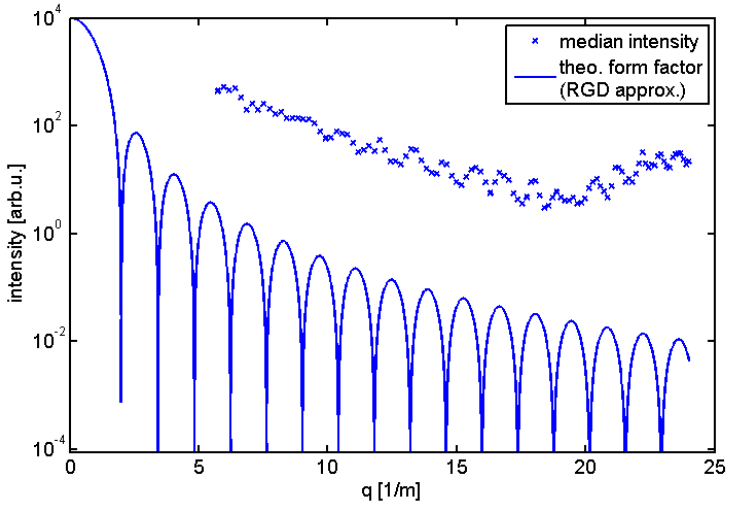

Figure 9: Dependence of the median of the scattered intensity from 4.5 µm polystyrene spheres on the wavevector transfer and the theorectical curve according to Reighley-Gans-Debye theory.

4.1.3 Very low concentrations

In order to illustrate the effect of a very low concentration of spheres, results from measurements of the 4.5 µm PS DL1 sample are discussed in this section. In principle, for the 4.5 µm spheres, very low concentrations have to be used to ensure that only single scattering takes place. In this case, however, the mean number of spheres in the scattering volume drops to the order of $\mathcal{O}(10^3)$, and correlations due to fluctuations in particle number are expected (see for example equation 28).
Figure 10 shows one measured g_2-function, with very low times already excluded, and a fitted curve according to equation 34.

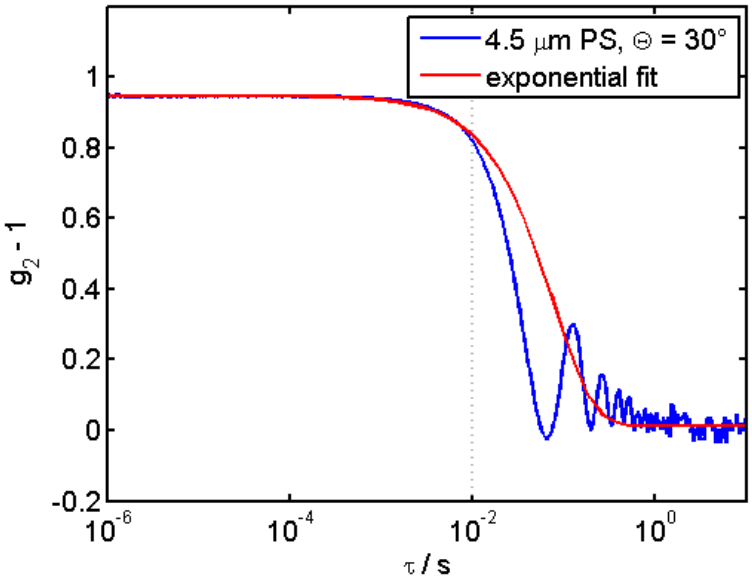

Figure 10: Measured g_2-function of 4.5 µm polystyrene spheres at 30° and a fit to the data.

Deviations from the expected exponential behaviour, in form of oscillations for higher delay times, are clearly visible. Comparison to figure 11, were the g_2-functions of the 4.5 µm spheres for different angles are plotted, as well as to the according figure 3 for the 2 µm particles, shows that the oscillations are most imminent for small angles. The reason is that for higher wavevector transfers, faster dynamics are probed. Due to the higher concentrations the oscillations are not unambiguously identified in the other samples. Nevertheless the oscillations might contribute to the noise at higher delay times.

Similarly, an unexpected behaviour is observable in the (uncorrelated) count rate of the photo-diode. In figure 12 the count rates of the two 4.5 µm samples (at an angle of 40°) are compared. Note that the absolute count rate is subject to the different attenuation of the laser used.
While for the higher concentrated sample, the count rate fluctuates predominantly on small timescales about the mean value (with correlations as given by the g_2-function),

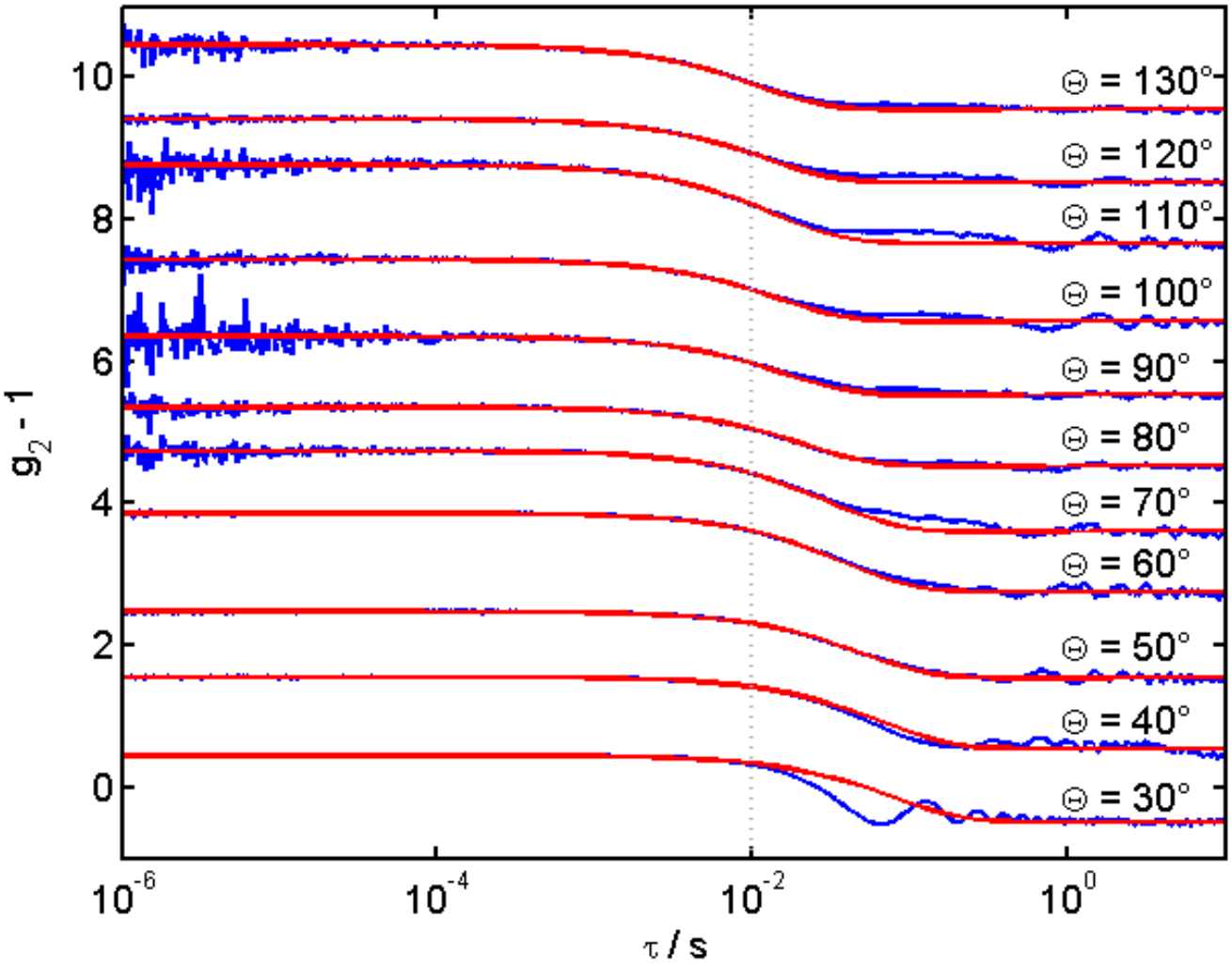

Figure 11: Measured g_2-functions of 4.5 µm polystyrene spheres in the angular range of 10° to 130° with corresponding fits to the data.

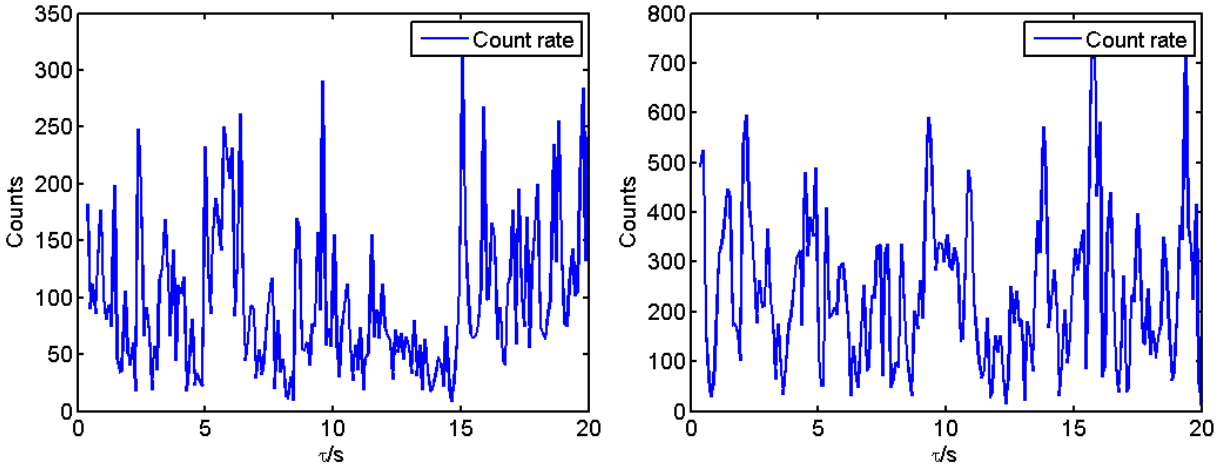

(a) Count rate of 4.5 µm PS DL1 sample with lower concentration of spheres.

(b) Count rate of 4.5 µm PS DL0 sample with higher concentration of spheres.

Figure 12: Count rate of photo-diode for higher and lower concentrated samples of polystyrene spheres.

for the sample with lower concentration, the count rate has fluctuations with a higher relative amplitude on larger timescales indicating insufficient statistics. Therefore, a meaningful determination of the hydrodynamical radius is not possible for very low concentrations, since the theory outlined in this work is not able to describe the behaviour sufficiently.
Due to the restrictions explained above, the use of DLS techniques to characterise particles of the size of several µm is limited. In principle it is possible, though, to further increase the intensity at the cost of multiple scattering, but minimise these effects by cross-correlation techniques [9]. This is however not part of this work.

4.1.4 The effect of isopropanole

In this section the effect of parasitic scattering is exemplified by samples in cuvettes, which were cleaned before use with isopropanole. In principle the isopropyl alcohol is expected to evaporate quickly, such that the sample is not contaminated. It is possible, however, that small remains stay in the cuvette and form droplets in the water used as a solution, which turned out to be the case here.
To illustrate this, figure 13a shows the g_2-function, of a - apart from the isopropanole - pure water sample. It appears quite similar to the correlation function of the polystyrene particles in water. Most importantly, the correlation decays on a comparable timescale, while pure water is expected to decay much faster. Due to the overlap of relaxation times this can strongly effect the characterisation measurements of the polystyrene microspheres. As an example, figure 13b shows the the relaxation rate of 2 µm polystyrene spheres in suspension with isopropanole present, which was determined via fits to the g_2-function like before. There are clear deviations from a linear behaviour visible. In

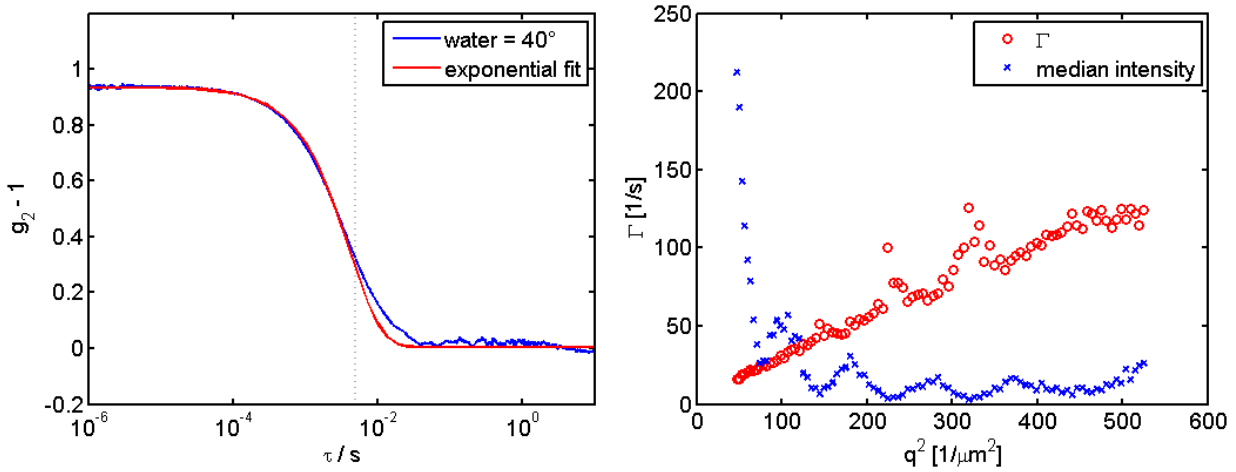

(a) g_2-function of a sample without polystyrene spheres.

(b) Correlation between the median scattered intensity and the relaxation rate

Figure 13: Effect of isopropanole vesicles remaining in the sample.

particular, modulations in the form of 'bumps' on top of the linear slope show up. To explain this, the median of the total scattered intensity is plotted (in arbitrary units) as well. It can be seen that an increase in the relaxation rate corresponds to a minimum in the scattered intensity. Therefore, whenever the scattered intensity of the polystyrene spheres, which in principle contribute most to scattering, is low, scattering from the isopropanole droplets becomes important, explaining the correlations between the relaxation rate and the scattered intensity. Thus, the cuvettes were not cleaned with isopropanole in all other measurements.

4.2 Speckles patterns

In this section the analysis of the images taken by the CCD camera is discussed. In figure 14 a typical speckle pattern taken by the CCD is shown. It depicts the intensity (in arbitrary units) scattered by the microspheres in the 4.5 µm PS DL0 sample into an angle of 15°. It was already corrected for dark field effects. Many elliptical intensity speckles are randomly distributed on the image and form the so-called speckle pattern. In addition to the speckles interference fringes, resulting from the optics used, show up, leading to modulations of the speckles.
To analyse the speckle patterns images of the scattered light of two different samples were recorded. In contrast to the point detector, the scattered intensity is not focused on the detector. Therefore, higher scattered intensities are needed to get a reliable signal. For this reason the stronger concentrated samples 2 µm PS DL0 and 4.5 µm PS DL0 were used. For the same reason it was not possible to cover the same angular range as in the case of a point detector. Data was taken in the range of 15° to 50° in steps of

5°[10].
In principle it has to be considered that the CCD chip covers a certain angular range. However, since the range is smaller than 1°, it will be assumed in the following that the angle is fixed on the whole chip.

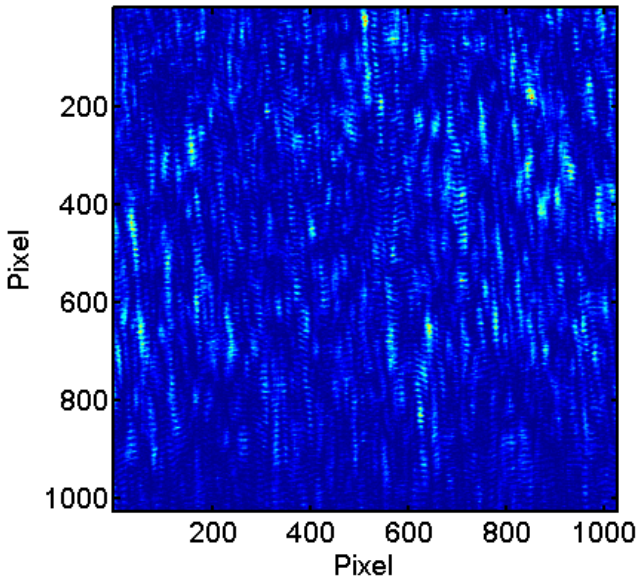

Figure 14: Example speckle pattern of light scattered by the 4.5 µm PS DL0 sample into an angle of 15°. The intensity is in arbitrary units.

From the size of the speckles and the statistics of the intensity distribution it is possible to extract information on the effective scattering volume and the coherence of the light source and the optics used, as will be explained in the following. Furthermore, similar to the previously discussed case of a point-detector, it is possible to relate intensity fluctuation in time to the dynamics of the system.

4.2.1 Speckle sizes

According to equation 40 the speckle size is inversely proportional to the effective (lateral) scattering region and has no direct dependence on particle size or scattering angle. In the case of single scattering and full coherence the effective scattering region is simply the laser spot size in the sample, while in the case of multiple scattering the effective volume gets larger and the speckles accordingly smaller. In figure 15 a section of 400x400 pixels of CCD images for 15° and 40° and both sphere sizes are shown.
While in vertical direction the speckles seem to be of comparable size for both angles and samples, in horizontal direction the speckles recorded at 40° are smaller than those recorded at 15°. This can be explained as follows: The laser impinging on the sample illuminates a volume characterised by $(\delta x, \delta y, l)$, where $(\delta x, \delta y)$ is the transverse spot

[10]For the 2 µm PS DL0 sample, due to too low intensities, no data was taken at an angle of 45°.

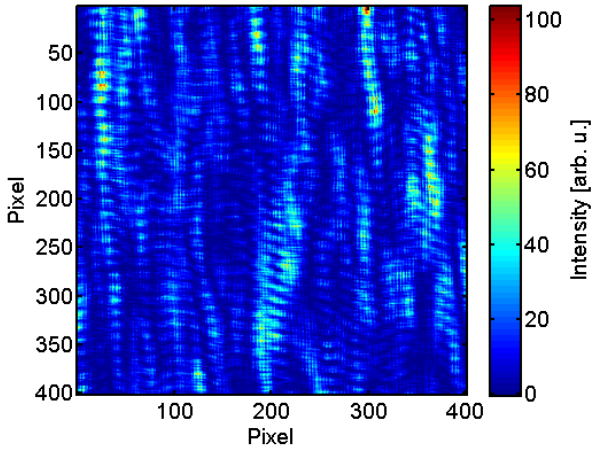

(a) 2 µm spheres at 15°

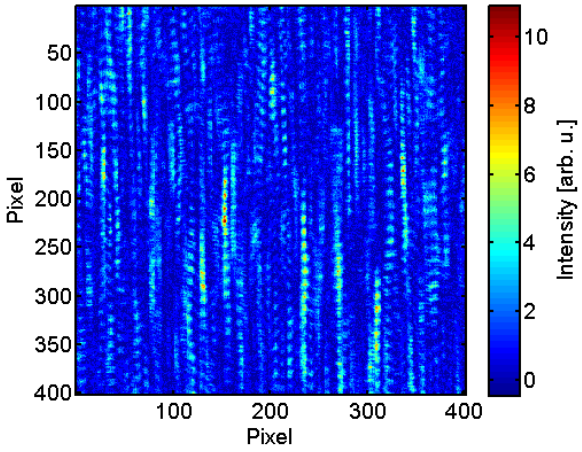

(b) 2 µm spheres at 40°

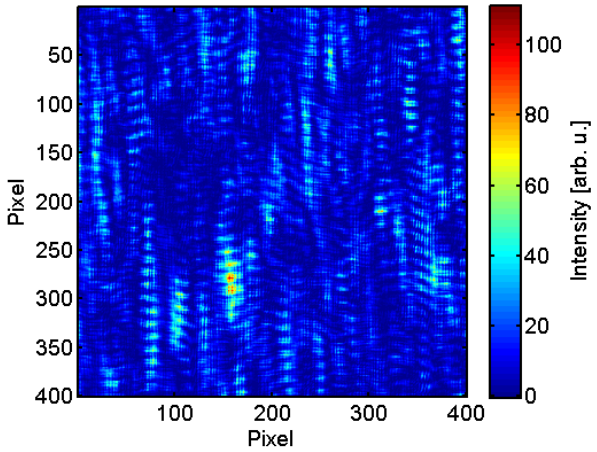

(c) 4.5 µm spheres at 15°

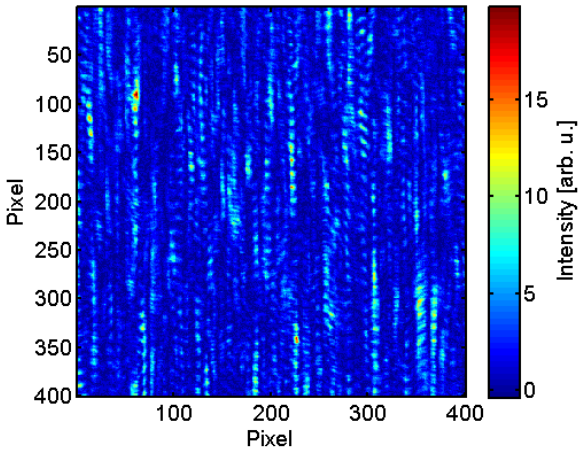

(d) 4.5 µm spheres at 40°

Figure 15: 400x400 pixels sections of the recorded speckle patters of 2 µm and 4.5 µm microsperes at scattering angles of 15° and 40°.

size of the laser (in horizontal and vertical direction respectively) and l is (or is related to) the length of the cuvette. In forward direction at an angle of $\theta = 0°$ the projection of the illuminated volume onto the plane of observation is simply the transverse spot size of the laser $(\delta x, \delta y)$. When observing at an angle of $\theta = 90°$ the projection of the illuminated volume in vertical direction is still given by the vertical spot size of the laser δy, while in horizontal direction the projection is now the length of the cuvette l. For an general angle the horizontal effective scattering region is given by

$$D_{hor} = \delta x \cos\theta + l \sin\theta. \tag{44}$$

To analyse the speckle size more quantitatively, the spatial autocorrelation function

$$C(\delta x, \delta y) = \frac{\langle I(x + \delta x, y + \delta y) I(x, y) \rangle_{px}}{\langle I \rangle_{px}^2}, \tag{45}$$

where $\langle \cdot \rangle_{px}$ denotes the average over all pixels, of one image for each recorded angle (and each sample) is computed. As an example the central section of the autocorrelation function for the 4.5 µm microsperes at 15° is shown in figure 16.

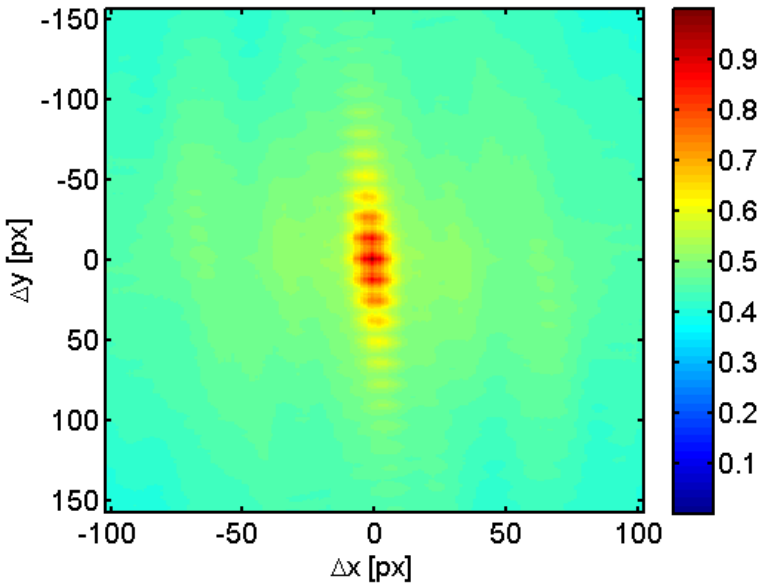

Figure 16: Central section of the autocorrelation function for 4.5 µm microsperes at 15°.

Since the speckles are randomly distributed, correlations between different speckles average to a constant background in the limit of an infinite number of speckles and therefore do not affect the image strongly. On the contrary, the interference fringes already present in figure 14 are regularly spaced and therefore clearly visible in figure 16. These fringes strongly affect the determination of the vertical speckle size. In figure 17 a horizontal and vertical cut through the autocorrelation function is plotted.

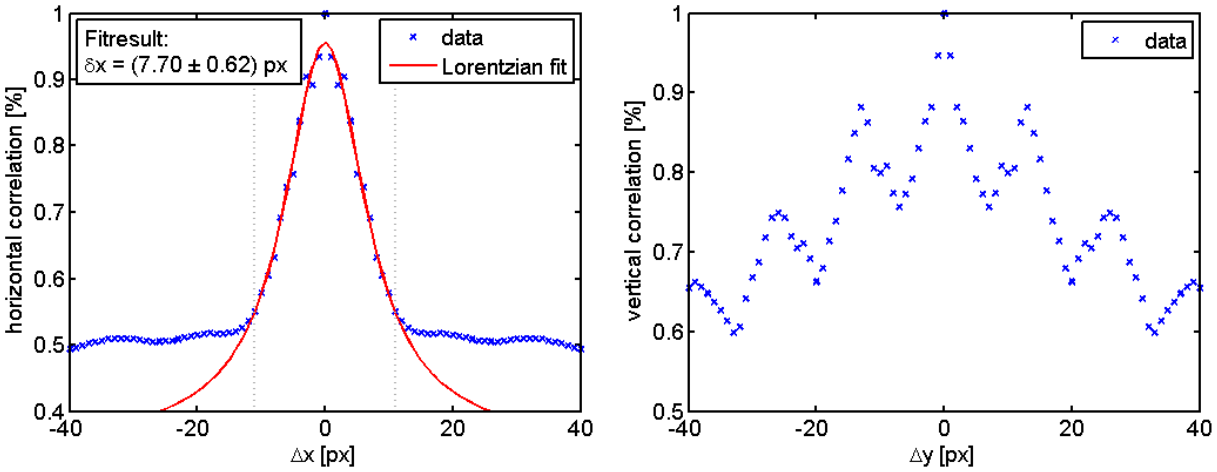

(a) Horizontal cut through the autocorrelation function with a fit to the data in the area indicated by the dotted vertical lines.

(b) Vertical cut through the autocorrelation function.

Figure 17: Horizontal and vertical cut through the autocorrelation function.

In the horizontal cut a clear peak is present. The peak in the autocorrelation of a speckle distribution takes the form of a Lorentzian, while some incoherent scattering which might be present increases the correlation at very low δx [15]. Limiting the discussion to the signal region ($\delta x = [-11, 11]$), using the model of a Lorentzian peak and excluding the data at $\delta x = 0, \pm 1$, the correlation function was fitted. The result is plotted in figure 18a. The fit suggests a horizontal speckle size of $\delta x = (7.70 \pm 0.62)$ px corresponding to an effective lateral scattering region of (5.5 ± 0.5) mm.
In the vertical cut, the effect of the fringes is imminent. Therefore it is not possible to determine the vertical speckle size by a fit to the data. To minimise the influence of the fringes, only single speckles are considered in the following, by defining an appropriate region of interest (ROI) in the speckle patterns. For this single speckle the autocorrelation function is computed again and the vertical and horizontal cut plotted, as shown in figure 18 for the previously considered example of 4.5 µm spheres and an angle of 15°.
As can be seen in figure 18, the Lorentzian model (with the central points already excluded) is still not able to describe all features of the data, especially for the vertical cut. However the fit results can at least give an estimate of the speckle size. To improve the estimate, instead of one, ten ROIs are defined and for each of them the speckle size is determined individually. In the end the average is taken. The results, for each angle and both samples, are summarised in table 6. For each angle the horizontal speckle size in once determined by a fit to the cut through the full autocorrelation function and, as a crosscheck, by the average of ten different single speckle sizes as explained above, while for the vertical speckle size only the latter method is possible[11].

[11]Note that a proper fit was not possible for single speckles in horizontal direction at an angle of 50° using the 4.5 µm spheres.

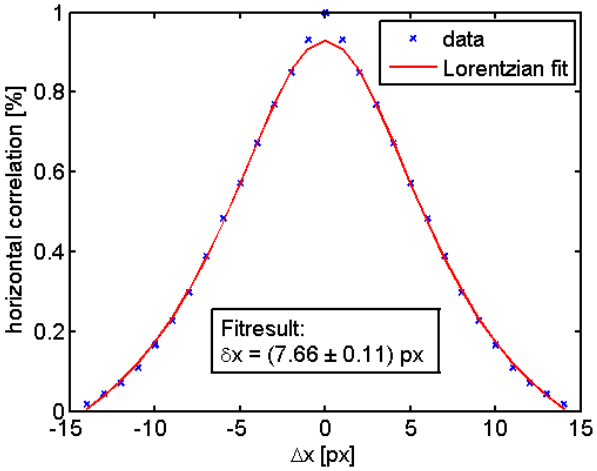

(a) Horizontal cut through the autocorrelation function with a fit to the data using a Lorentzian model.

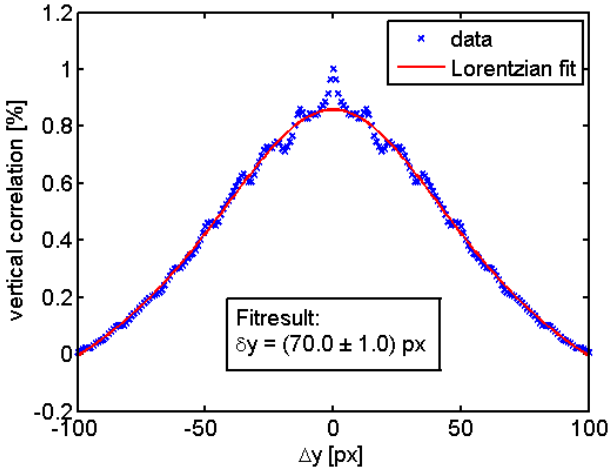

(b) Vertical cut through the autocorrelation function with a fit to the data using a Lorentzian model.

Figure 18: Horizontal and vertical cut through the autocorrelation function of a single speckle.

		hor. full autocor.	hor. ROI	vert. ROI
2 µm	**15°**	(8.927 ± 1.715) px	(9.290 ± 1.051) px	(58.9 ± 10.3) px
	20°	(6.639 ± 0.423) px	(7.810 ± 0.838) px	(60.0 ± 10.5) px
	25°	(5.452 ± 0.267) px	(6.042 ± 0.961) px	(60.9 ± 9.0) px
	30°	(4.284 ± 0.244) px	(5.578 ± 0.808) px	(60.2 ± 3.0) px
	35°	(2.960 ± 0.504) px	(5.019 ± 0.765) px	(60.1 ± 6.4) px
	40°	(2.806 ± 0.392) px	(5.315 ± 0.975) px	(58.3 ± 8.5) px
	50°	(0.516 ± 0.058) px	(4.341 ± 1.256) px	(57.8 ± 6.2) px
4.5 µm	**15°**	(7.693 ± 0.617) px	(8.631 ± 0.669) px	(56.6 ± 12.9) px
	20°	(5.805 ± 0.197) px	(7.485 ± 1.132) px	(59.5 ± 6.9) px
	25°	(4.022 ± 0.234) px	(5.804 ± 0.736) px	(51.2 ± 9.9) px
	30°	(3.134 ± 0.219) px	(5.209 ± 0.940) px	(55.9 ± 7.6) px
	35°	(4.097 ± 0.146) px	(4.295 ± 0.838) px	(55.0 ± 9.3) px
	40°	(3.334 ± 0.266) px	(4.761 ± 0.917) px	(57.0 ± 5.4) px
	45°	(3.097 ± 0.327) px	(4.433 ± 0.591) px	(62.1 ± 7.7) px
	50°	(2.14 ± 0.26) px	—	(59.2 ± 6.5) px

Table 6: Lateral speckle sizes determined by a fit to the cut through the autocorrelation function of the full image in horizontal direction, and several ROIs in horizontal and vertical direction.

As expected, the vertical speckle size is, within its error, the same for all angles. Because the size coincides for both sphere sizes as well, it can be concluded that multiple scattering is negligible for the (in principle slightly opaque) 4.5 µm PS DL0 sample. The results are plotted in figure 19b, where the average, and the standard deviation are indicated as well. The vertical speckle size was determined to be $\delta y = (58.2 \pm 2.8)$ px corresponding to a vertical effective scattering region of

$$D = (0.72 \pm 0.04)\,\text{mm}.$$

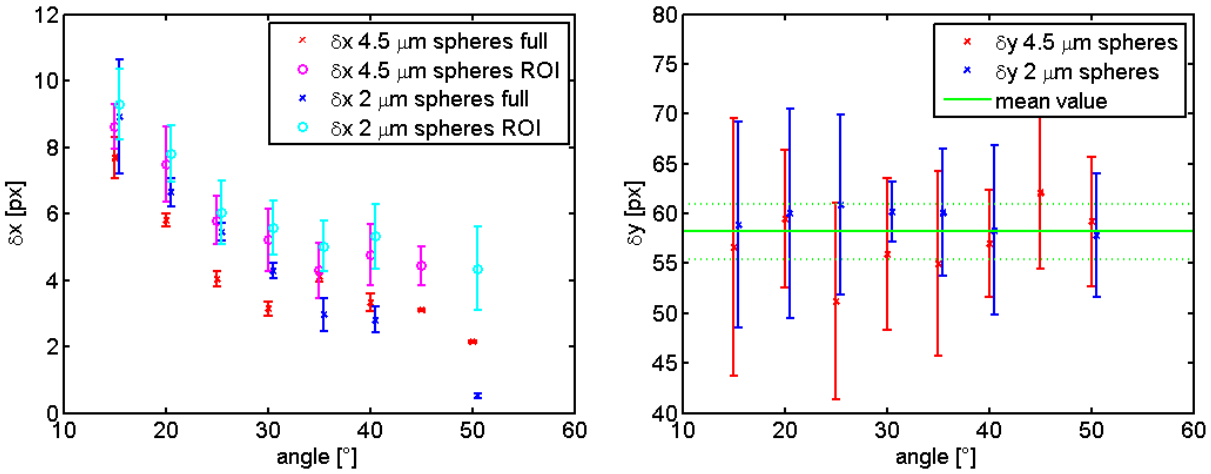

(a) Horizontal speckle sizes for both samples.

(b) Vertical speckle sizes for both samples.

Figure 19: Horizontal and vertical speckle sizes.

The results from the determination of the horizontal speckle size for the different methods are plotted in figure 19a where a clear trend of decreasing speckle size with increasing angle is visible. It has to be taken into consideration that for wider angles the speckle extension is on the order of a single pixel and the reliability of the fits has to be doubted. At least for small angles the results from the different methods and samples are comparable although the fit to single speckles gives a larger speckle size in general. This might be because of poor separation of speckles in horizontal direction. Although the trend of decreasing speckle size is clear a determination of the horizontal effective scattering region according to equation 44 is not possible, due to a too large spread of the data.

4.2.2 Dynamics

Similar to the method using a point detector described in section 4.1, it is possible to determine the g_2-function using CCD data. To this end a sequence of images with a certain framerate is recorded. As a next step each pixel is correlated with the same pixel some time step τ later and the average over all pixels is taken. The result is the so-called two-times correlation function

$$C_I(q,t,\tau) = \frac{\langle I_{px}(q,t) I_{px}(q,t+\tau)\rangle_{px}}{\langle I_{px}(q,t)\rangle_{px}\,\langle I_{px}(q,t+\tau)\rangle_{px}}. \tag{46}$$

To arrive at the g_2-function, the time average is taken

$$g_2(q,t) = \langle C_I(q,t,\tau) \rangle_t \,. \tag{47}$$

The advantage of using a two-dimensional detector compared to a point detector are the significantly larger statistics with a single measurement, since an average over many pixels (1024x1024 in this case) is taken. However, it is not possible to probe very fast dynamics, since the CCD framerate is limited to 120 fps. The advantages and disadvantages will be illustrated in the following.
Due to technical limitations it is only possible to take 100 consecutive images with the CCD camera in use. Therefore, for each angle and sample, two separate measurements are performed to cover the whole time range of interest. 100 pictures are taken with a framerate of 119.8 fps and another 100 with a framerate of 20.0 fps. The exposure time of a single image is 2000 µs in both cases. The effect of a finite integration time - as long as it is much smaller than the relaxation time - was shown to not affect the form of the g_2-function, although slightly altering the contrast [16].
The resulting g_2-functions (the 120 fps and the 20 fps measurements already combined) are plotted and fitted by the same exponential model used for the point detector data. In figure 20, as an example, the plots for different angles are shown for both samples. For comparison the data from the point detector is plotted as well and the constant background is subtracted for both data sets.
As expected, there are significantly less fluctuations at larger delay times ($\tau \gtrsim 10^{-1}$ s) due to the better statistics. On the contrary, caused by the limited framerate, only delay times $\tau \gtrsim 10^{-2}$ s are probed. Furthermore, the contrast determined by the fit varies significantly between the point detector and the CCD data, where the time resolution in not good enough to see the 'plateau' at small delay times. This has the effect that g_2-curves describing the same relaxation rate (within its error) might look quite different as is the case in figure 20b. The contrast will be discussed further in section 4.2.3.
While the relaxation rates for the 2 µm spheres appear to be of the same order for both measurements, for the larger 4.5 µm spheres the relaxation rate determined by the CCD methods is in general faster than the rate determined with the point detector. Furthermore, for the delay times considered here and slower dynamics probed (that is a lower wavevector transfer and therefore a smaller angle) the data is not fully described by a single exponential (see figure 20c). In contrast to the data taken by the photodiode the two-dimensional data offers an additional possibility to check whether the time averaging leading to the g_2-function is valid, or whether additional dynamics, not described by the current approximation scheme, are present. To this end the two-times correlation function is plotted for both samples and an angle of 15° in figure 21.
The g_2-function corresponds to an averaging of diagonal cuts through the C_I-function. The figure shows that a proper determination of the g_2-function is problematic in both cases, since there are additional dynamics present. The effect is clearly stronger for the 4.5 µm spheres, however. The modulations are an indication for additional non-equilibrium processes, like for example sedimentation of the spheres, or vibrations in the

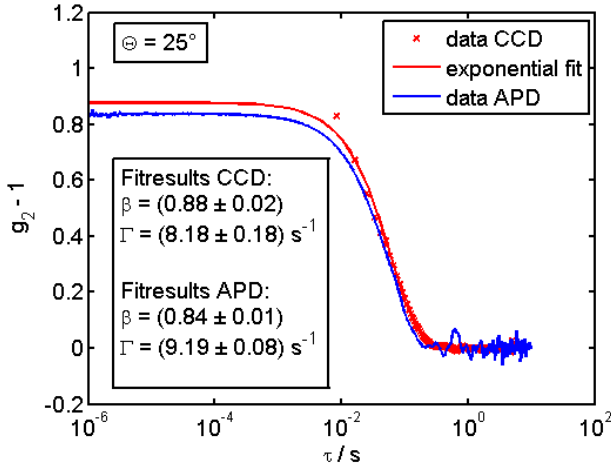

(a) 2 µm sample at 25°

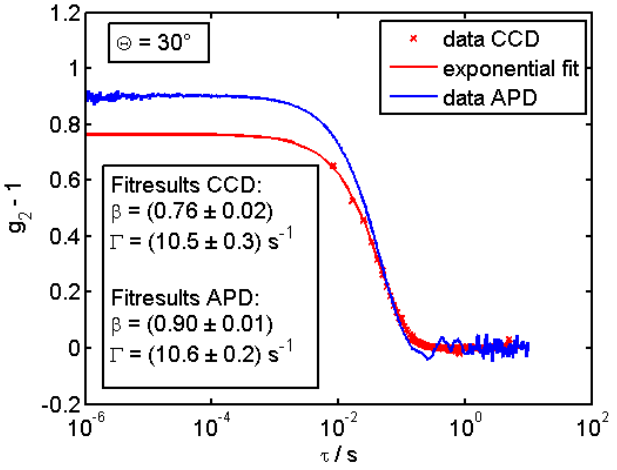

(b) 2 µm sample at 30°

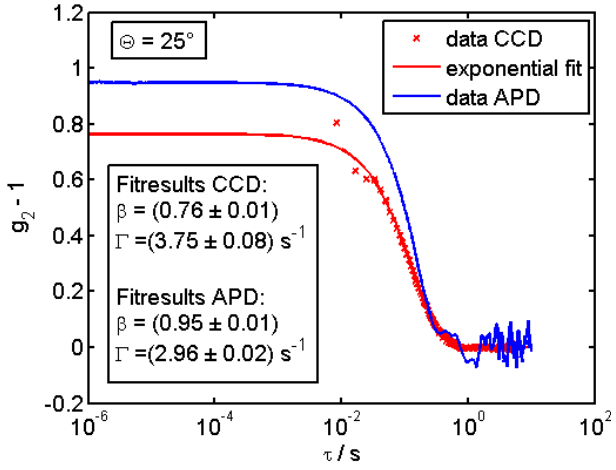

(c) 4.5 µm sample at 25°

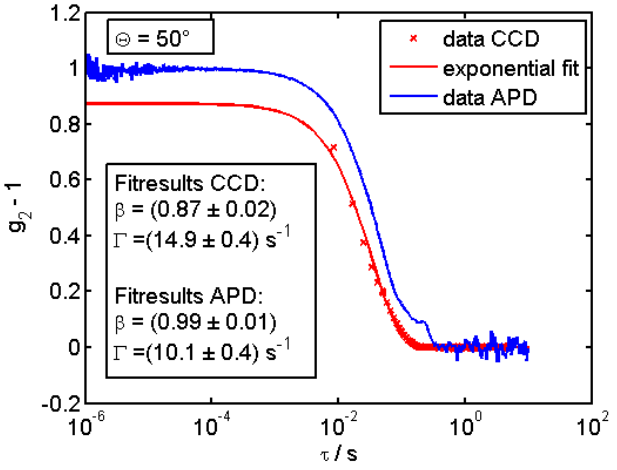

(d) 4.5 µm sample at 50°

Figure 20: g_2-function of both samples determined with the CCD detector and the APD at different angles.

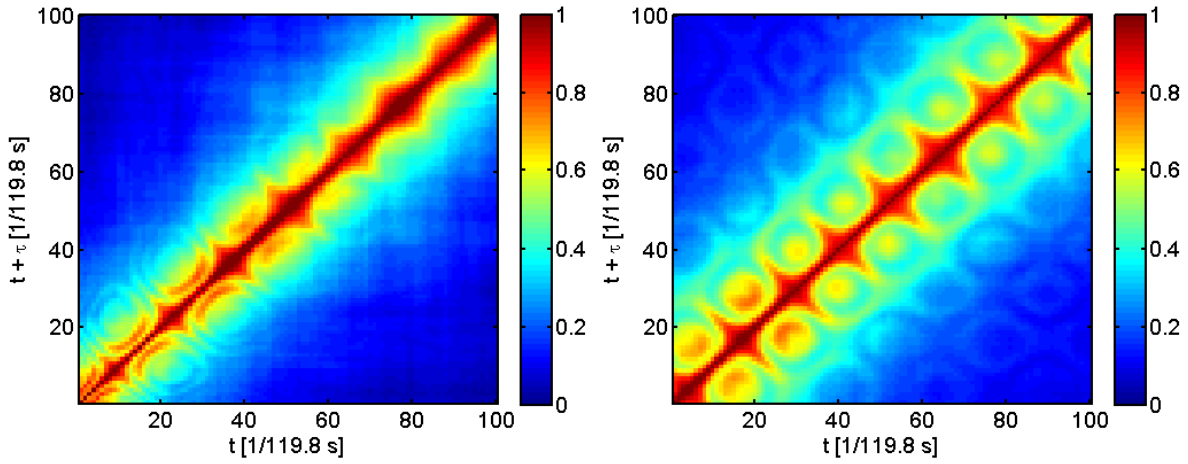

(a) C_I-function of 2 µm spheres at 15°. (b) C_I-function of 4.5 µm spheres at 15°.

Figure 21: Two-times correlation function for both samples at an angle of 15°. For clarity, the images were extended to negative time delays τ by mirroring them at the diagonal.

setup [12]. Note that these effects cannot be identified by a point detector alone.
In figure 22 the determined relaxation rates are plotted against the corresponding wavevector transfer. The corresponding data from the point detector is plotted for reference as well.
Note that the uncertainty on the relaxation rate for the smaller particles at angles is quite high, since the laser beam was strongly attenuated to be able to cover the full angular range covered by the CCD.
For the 2 µm spheres the resulting hydrodynamic radii are determined to be

$$R_h = (0.95 \pm 0.05)\,\mu\text{m}$$

using the CCD camera and

$$R_h = (1.10 \pm 0.11)\,\mu\text{m}$$

using the photodiode. This has to be compared to the previous measurement using the photodiode yielding a radius of

$$R_h = (1.03 \pm 0.03)\,\mu\text{m}$$

and the actual sphere radius of

$$R = (0.97 \pm 0.03)\,\mu\text{m}.$$

All radii are compatible within their errors, while the radius determined in 4.2.2 has the highest uncertainty due to the aforementioned low intensity at wide angles.

[12] The effects from vibrations might be enhanced by the resulting oscillations of the interference fringes present on the images.

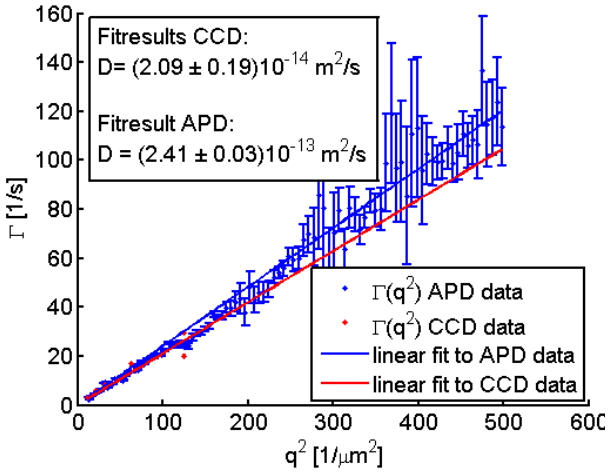

(a) Γ plotted against q^2 for 2 µm spheres.

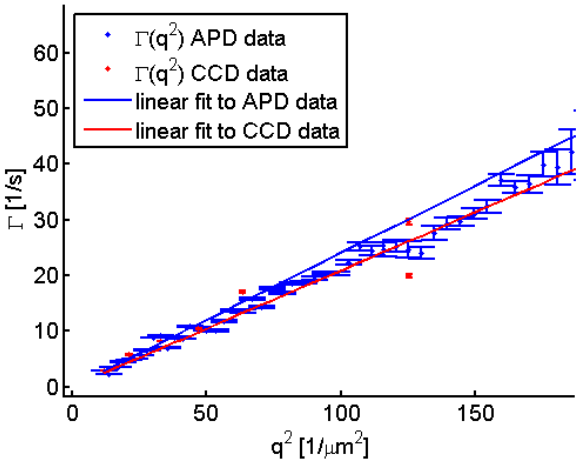

(b) Γ plotted against q^2 for 2 µm spheres. Zoom to low q^2.

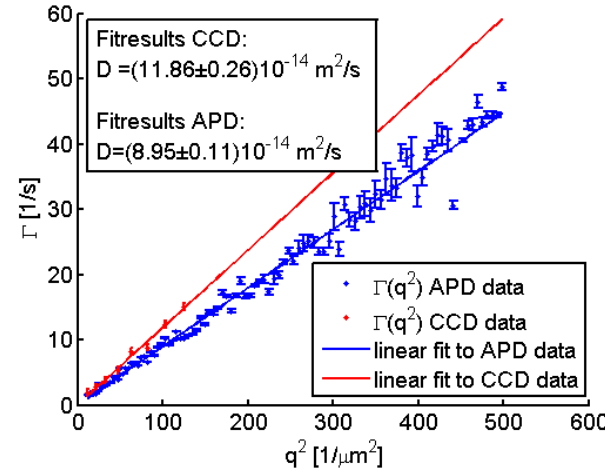

(c) Γ plotted against q^2 for 4.5 µm spheres.

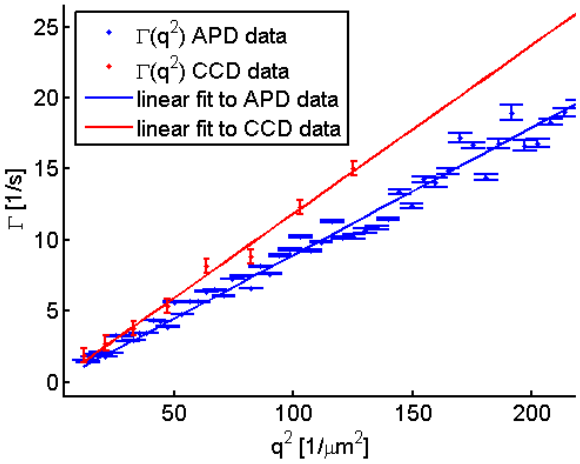

(d) Γ plotted against q^2 for 4.5 µm spheres. Zoom to low q^2.

Figure 22: Relaxation rate plotted against the squared wave vector transfer. Data from both the CCD camera and the APD is shown. The data were fitted using a linear model.

For the 4.5 µm spheres the resulting hydrodynamic radii are determined to be

$$R_h = (1.94 \pm 0.10)\,\mu\text{m}$$

using the CCD camera and

$$R_h = (2.56 \pm 0.13)\,\mu\text{m}$$

using the photodiode. This has to be compared to the previous measurement using the photodiode yielding a radius of

$$R_h = (2.54 \pm 0.11)\,\mu\text{m}$$

and the actual sphere radius of

$$R = (2.26 \pm 0.08)\,\mu\text{m}.$$

The two measurements with the APD coincide with each other and are compatible with the actual radius within the 3σ range as stated before. The radius determined by the CCD data is smaller than the other radii. As stated before, all those results for the 4.5 µm spheres have to be treated with care.

4.2.3 Contrast

The contrast β gives information about the coherence of the light source and the optics used. In the case considered here, where a laser in the visible range is used, it can be assumed that the laser is fully coherent and the significant part of the incoherent radiation is due to the optics. Sources of incoherence could be dust and dirt on some optical components, their finite aperture or stray light. Nevertheless a high contrast is to be expected.
It is possible to extract the contrast from the fitted g_2-function. Because of the larger statistics the data taken with the CCD is better suited to this end, since in the case of a point detector parasitic scattering may lead to fluctuations of the contrast (even a - in principle unphysical - contrast larger than one is possible, see section 4.1). The fluctuations are less present when using CCD data. With the data and the fits illustrated in the previous section 4.2.2 a contrast of

$$\beta = 0.83 \pm 0.02$$

is obtained, assuming that the contrast is independent of angle and particle size. Usually, another possibility to determine the contrast is by making use of equation 37 stating that the contrast is given by the quotient of standard deviation of the intensity and its mean value. However, this method is not well suited for low intensity speckles where the non-continuous intensity scale can strongly effect the outcome. Therefore the contrast was not determined using this method in this work. Finally, the probability distribution of the intensity $P(I)$ given by equation 36 is dependent on the number of coherence volumes M and therefore, related by equation 39, the contrast.

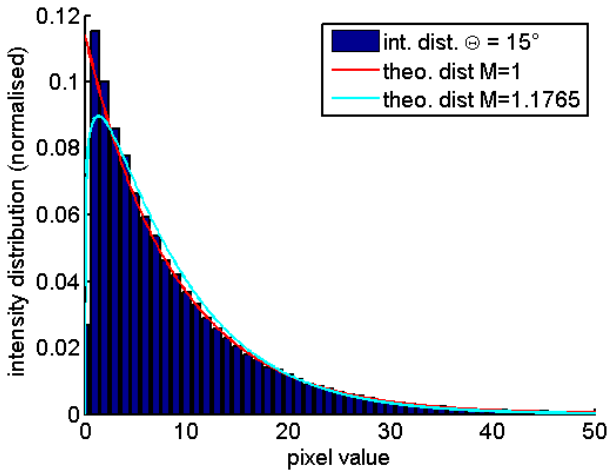

(a) 2 µm spheres and $\Theta = 15°$.

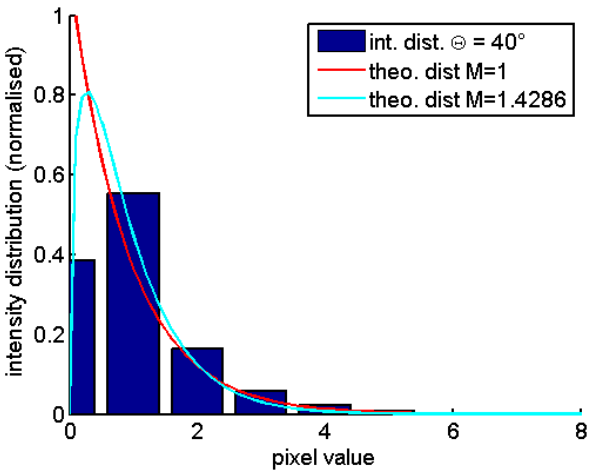

(b) 2 µm spheres and $\Theta = 40°$.

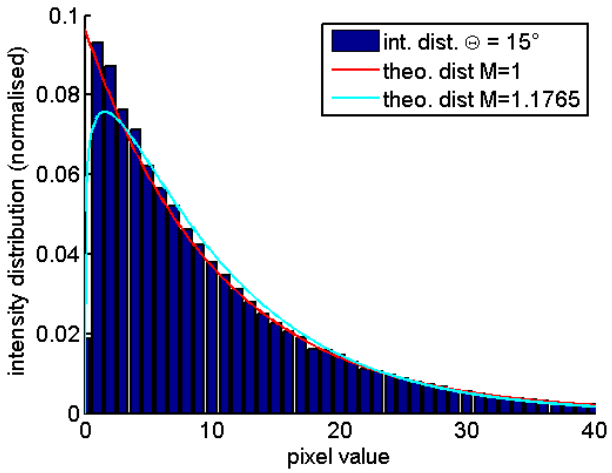

(c) 4.5 µm spheres and $\Theta = 15°$.

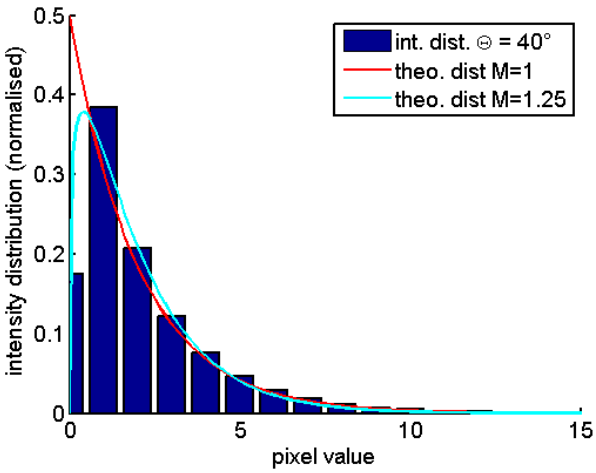

(d) 4.5 µm spheres and $\Theta = 40°$.

Figure 23: Measured intensity distribution for both samples and different angles together with theoretical curves corresponding to different values of M.

Figure 23 shows the distribution of the intensities for both samples for angles of 15° and 30°. The theoretical curves for full coherence ($M = 1$) and a contrast of 70%-85% ($M = 1.1765 - 1.4286$) are shown as well. The distribution mostly follows the exponential (i.e. full coherence) curve with the exception, that the pixel value of zero is strongly suppressed and intensity shifted to a value of 1. With the dark-field already subtracted, this might be a remaining noise effect. A meaningful fit to the data is not possible due to this reason. However, the data supports in principle a higher contrast close to 1 rather than the 83% determined by the fits to the g_2-function.

4.2.4 Comparison

As illustrated before, the clear advantage of using a CCD detector is the better statistics and therefore less noise. Furthermore this has the consequence of reduced measuring times. The intensity correlation was recorded with the photodiode for 60 s for each angle while the CCD images where taken within approximately 6 s (100 images with 120 fps and 100 images with 20 fps). Therefore the bare measuring time is reduced by a factor of 10. Apart from the time savings this has the advantage of being less influenced by long timescale effects, like the sedimentation of the spheres. Furthermore, with a space resolved detector it is possible, if needed, to observe spatial correlations in addition to temporal ones.
Disadvantages of using a CCD detector are the restrictions to slower dynamics and due to the lower dynamical range of the CCD to a smaller angular range. Typical dynamics for the microspheres at these low angles have a relaxation rate on the order of $\Gamma = 1\,\mathrm{s}^{-1}$ to $30\,\mathrm{s}^{-1}$ which can be partly, but not fully, resolved, as can be seen in figure 20. Wider angles and therefore faster dynamics cannot be covered properly for this reason. In principle it would be possible, though, to decrease the relaxation rate by replacing the water by another solvent having a larger viscosity (e.g. glycerol) and thus decreasing the dynamics.
For the 2 µm spheres considered here the use of an APD as a detector showed to be fully sufficient and due to the larger angular range covered and the possibility to use lower concentrated samples the preferable method. Nevertheless using a CCD detector is possible as well and gives, in addition to some information on the contrast and the scattering volume, compatible results. DLS methods are not fully suited to characterise the 4.5 µm spheres. The data taken with the CCD is an important crosscheck to arrive at this conclusion.

5 Summary and Conclusion

In this work, microspheres were characterized by DLS methods. The methods and the corresponding approximation schemes are originally designed for smaller nanoparticles. Therefore the samples containing polystyrene spheres close to the very edge of the applicability of DLS. For this reason, crosscheck measurements using a CCD detector were conducted in addition to the usual point detector measurements. While for the smaller 2 µm spheres all relevant approximations seem to hold (at least approximately) and it was still possible to determine the hydrodynamical radius, for 4.5 µm spheres the applicability of DLS methods were shown to be very limited. Nevertheless, at least a rough estimate of the particle size was determined. Furthermore advantages and disadvantages of different time-correlation methods were discussed.

References

[1] Berne, B. J., and Pecora, R. *Dynamic light scattering: with applications to chemistry, biology, and physics.* Dover Publications, Mineola (2000).

[2] Kotlarchyk, M., Sow-Hsin Chen, and Shoji Asano. *Accuracy of RGD approximation for computing light scattering properties of diffusing and motile bacteria.* App. opt., 18.14 (1979).

[3] Schmitz, K. S. *An introduction to dynamic light scattering of macromolecules.* Academic Press Inc., San Diego (1990)

[4] Schaefer, D. W., and Berne, B. J. *Light scattering from non-Gaussian concentration fluctuations.* Phys. Re. Lett., 28.8 (1972).

[5] Nolting, W. *Grundkurs Theoretische Physik 7.* Springer, Heidelberg (2005).

[6] Schroer, M. A. *Small angle X-ray scattering studies on proteins under extreme conditions.* Diss., TU Dortmund (2011).

[7] Lang, P. *Scattering Methods: Basic Principles and Application to Polymer and Colloidal Solutions.* Lec. Notes, HHU Düsseldorf (2011): `http://www.fz-juelich.de/SharedDocs/Downloads/ICS/ICS-3/EN/Lang_002.pdf?__blob=publicationFile`, as of September 2015

[8] Pecora, R. *Basic concepts. Scattering and time correlation functions.* In: Soft Matter Characterization. Springer, New York (2008).

[9] Chu, B. *Dynamic light scattering.* In: Soft Matter Characterization. Springer, New York (2008).

[10] Grübel, G.,Madsen A., and Robert A. *X-ray photon correlation spectroscopy (XPCS).* In: Soft Matter Characterization. Springer, New York (2008).

[11] Goodman, Joseph W. *Some fundamental properties of speckle.* J. Opt. Soc. Am., 66.11 (1976).

[12] Schleitzer, S. *Dynamics of Soft Nanoparticle Dispersions studied by Dynamic Light Scattering and Photon Correlation Imaging.*Diploma Thesis, University of Clausthal (2011).

[13] Zajac, A., and Hecht, E.. *Optics, Fourth Edition.* Pearson Higher Education (2003).

[14] `http://www.thermexcel.com/english/tables/eau_atm.htm`, as of September 2015

[15] Als-Nielson, J., and McMorrow, D. *Elements of Modern X-Ray Physics.* John Wiley & Sons, Chichester (2011).

[16] Lumma, D., Lurio, L. B., Mochrie, S. G. J., and Sutton, M. *Area detector based photon correlation in the regime of short data batches: Data reduction for dynamic x-ray scattering.* Rev. Sci. Instrum., 71.9 (2000).

[17] Chen, S-H., Holz, M., and Tartaglia, P. *Quasi-elastic light scattering from structured particles.* App. opt, 16.1 (1977).

[18] Robert, A. *Dynamic behavior of charge stabilized colloidal suspensions.* Diss., UJF Grenoble (2001).

[19] Berry, G. C. *Total Intensity Light Scattering from Solutions of Macromolecules.* In: Soft Matter Characterization. Springer, New York (2008).

[20] Narayanan, T. *Synchrotron small-angle X-ray scattering.* In: Soft matter characterization. Springer, New York (2008).

[21] Conrad, H. *Dynamics of colloids in molecular glass forming liquids studied via X-ray photon correlation spectroscopy.* Diss., Univ. Hamburg (2014).

[22] Goldfischer, L. I. *Autocorrelation function and power spectral density of laser-produced speckle patterns.* J. Opt. Soc. Am., 55.3 (1965).